

Mirabbos Hojamberdiev, Ronald Vargas, Zukhra C. Kadirova, Kosaku Kato, Hadi Sena, Aleksei G. Krasnov, Akira Yamakata, Katsuya Teshima, Martin Lerch

## Unfolding the role of B site-selective doping of aliovalent cations on enhancing sacrificial visible light-induced photocatalytic H<sub>2</sub> and O<sub>2</sub> evolution over BaTaO<sub>2</sub>N

Open Access via institutional repository of Technische Universität Berlin

### Document type

Journal article | Accepted version

(i. e. final author-created version that incorporates referee comments and is the version accepted for publication; also known as: Author's Accepted Manuscript (AAM), Final Draft, Postprint)

### This version is available at

<https://doi.org/10.14279/depositonce-15604>

### Citation details

Hojamberdiev, M., Vargas, R., Kadirova, Z. C., Kato, K., Sena, H., Krasnov, A. G., Yamakata, A., Teshima, K., Lerch, M. (2022). Unfolding the Role of B Site-Selective Doping of Aliovalent Cations on Enhancing Sacrificial Visible Light-Induced Photocatalytic H<sub>2</sub> and O<sub>2</sub> Evolution over BaTaO<sub>2</sub>N. In ACS Catalysis (Vol. 12, Issue 2, pp. 1403–1414). American Chemical Society (ACS). <https://doi.org/10.1021/acscatal.1c04547>.

### Terms of use

This work is protected by copyright and/or related rights. You are free to use this work in any way permitted by the copyright and related rights legislation that applies to your usage. For other uses, you must obtain permission from the rights-holder(s).

# Unfolding the Role of *B*-Site-Selective Doping of Aliovalent Cations on Enhancing Sacrificial Visible-Light-Induced Photocatalytic H<sub>2</sub> and O<sub>2</sub> Evolution over BaTaO<sub>2</sub>N

Mirabbos Hojamberdiev<sup>1,2,\*</sup>, Ronald Vargas<sup>3</sup>, Zukhra C. Kadirova<sup>4,5</sup>, Kosaku Kato<sup>6</sup>, Hadi Sena<sup>7</sup>, Aleksei G. Krasnov<sup>8</sup>, Akira Yamakata<sup>6</sup>, Katsuya Teshima<sup>2,9</sup>, and Martin Lerch<sup>1</sup>

<sup>1</sup>*Institut für Chemie, Technische Universität Berlin, Straße des 17. Juni 135, 10623 Berlin, Germany*

<sup>2</sup>*Department of Materials Chemistry, Shinshu University, 4-17-1 Wakasato, Nagano 380-8553, Japan*

<sup>3</sup>*Instituto Tecnológico de Chascomús (INTECH) - Consejo Nacional de Investigaciones Científicas y Técnicas (CONICET) / Universidad Nacional de San Martín (UNSAM), Avenida Intendente Marino, Km 8,2, (B7130IWA), Chascomús, Provincia de Buenos Aires, Argentina*

<sup>4</sup>*Department of Inorganic Chemistry, National University of Uzbekistan, 100174 Tashkent, Uzbekistan*

<sup>5</sup>*Uzbekistan-Japan Innovation Center of Youth, University Street 2B, 100095 Tashkent, Uzbekistan*

<sup>6</sup>*Graduate School of Engineering, Toyota Technological Institute, 2-12-1 Hisakata, Tempaku, Nagoya 468-8511, Japan*

<sup>7</sup>*Center for Integrated Research of Future Electronics, Nagoya University, Aichi 464-8601, Japan*

<sup>8</sup>*Institute of Chemistry, Federal Research Center Komi Science Center, Ural Branch, Russian Academy of Science, Syktyvkar 167982, Russian Federation*

<sup>9</sup>*Research Initiative for Supra-Materials, Shinshu University, 4-17-1 Wakasato, Nagano 380-8553, Japan*

---

\*Corresponding author: E-mail addresses: khujamberdiev@tu-berlin.de and hmirabbos@gmail.com (M. Hojamberdiev)

**ABSTRACT:**

Doping of foreign cations and anions is one of the effective strategies for engineering the defects and modulating the optical, electronic, and surface properties that directly govern the photocatalytic O<sub>2</sub> and H<sub>2</sub> evolution reactions. BaTaO<sub>2</sub>N (BTON) is a promising 600-nm-class photocatalyst because of its absorption of visible light up to 660 nm, small band gap ( $E_g = 1.9$  eV), appropriate valence band-edge position for oxygen evolution, good stability under light irradiation in concentrated alkaline solutions, and nontoxicity. Although the photocatalytic and photoelectrochemical water splitting efficiencies of BaTaO<sub>2</sub>N have been progressively improved, it is still far from the requirements set for practical applications. Here, we employ a 5% *B*-site-selective doping of aliovalent metal cations (Al<sup>3+</sup>, Ga<sup>3+</sup>, Mg<sup>2+</sup>, Sc<sup>3+</sup>, and Zr<sup>4+</sup>) to enhance sacrificial visible-light-induced photocatalytic H<sub>2</sub> and O<sub>2</sub> evolution over BaTaO<sub>2</sub>N. The results of physicochemical characterizations reveal that no significant change in crystal structure, crystal morphology, and optical absorption edge is observed upon cation doping. Therefore, the difference observed in the O<sub>2</sub> and H<sub>2</sub> evolution during the photocatalytic reactions over pristine and doped BaTaO<sub>2</sub>N photocatalysts is explained by involving the optical, electronic, and surface properties. Also, molecular dynamics (MD) is used to gain insights into the respective effect of cation doping on adsorption energy of water molecules and formed intermediates (H\* for H<sub>2</sub> evolution and HO\*, O\* and HOO\* for O<sub>2</sub> evolution) on the BaTaO<sub>2</sub>N surfaces terminated with TaO<sub>6</sub>, TaN<sub>6</sub>, and TaO<sub>4</sub>N<sub>2</sub> octahedra. Finally, the experimental reaction rates for H<sub>2</sub> and O<sub>2</sub> evolution are correlated well using a linear energy-performance relationship, elucidating the doping and surface-termination trends observed in the BaTaO<sub>2</sub>N photocatalysts.

**KEYWORDS:** Oxynitrides; BaTaO<sub>2</sub>N; Doping; Water splitting; Photocatalysis; Molecular modeling; Adsorption energy

## 1. INTRODUCTION

Unlike their oxide counterparts, mixed-anion compounds exhibit unique electronic and atomic structures and physicochemical properties that can be effectively tuned by changing their anionic features specifically for energy conversion.<sup>1-3</sup> Recent studies have discovered various key characteristics of mixed-anion compounds, which cannot be otherwise observed in single-anion analogs.<sup>4-6</sup> Among them, transition-metal oxynitrides with perovskite-type structures are an emerging class of mixed-anion compounds with interesting optoelectronic, photocatalytic, photoelectrochemical, dielectric, and magneto-resistive properties that are sensitive to the surface local structure and oxide-nitride anion ordering.<sup>7-10</sup>

As a typical representative of the  $AB(O,N)_3$  perovskites, cubic  $BaTaO_2N$  is regarded as one of the promising 600-nm-class photocatalysts due to its absorption of visible light up to 660 nm, small band gap ( $E_g = 1.9$  eV), appropriate valence band-edge position for oxygen evolution achieved by a 4-electron transfer ( $4HO^- \rightarrow 4e^- + 2H_2O + O_2$ ), good stability under light irradiation in concentrated alkaline solutions, and nontoxicity.<sup>11</sup> The Co cocatalyst-modified  $BaTaO_2N$  photoanode prepared by a particle transfer method generated a photocurrent of  $4.2 \text{ mA}\cdot\text{cm}^{-2}$  at 1.2 V vs. reversible hydrogen electrode (RHE) under simulated sunlight.<sup>12</sup> The  $FeNiO_x$  cocatalyst-modified  $Ta_3N_5$ -nanorods/ $BaTaO_2N$  photoanode fabricated by combining glancing angle deposition and dip coating techniques yielded a photocurrent of  $\sim 4.5 \text{ mA}\cdot\text{cm}^{-2}$  at 1.2 V vs. RHE under simulated sunlight.<sup>13</sup> The  $CoO_x$ -deposited  $BaTaO_2N/Ta_2N/Ta$  photoanodes produced a photocurrent of  $4.6 \text{ mA}\cdot\text{cm}^{-2}$  at 1.2 V vs. RHE and exhibited a 9% IPCE at 600 nm during water oxidation under simulated sunlight.<sup>14</sup> Further, an unprecedented photocurrent of  $6.5 \text{ mA}\cdot\text{cm}^{-2}$  at 1.23 V vs. RHE was achieved for Ar-annealed  $BaTaO_2N$  during sunlight-driven water oxidation.<sup>15</sup>

Although the photocatalytic and photoelectrochemical water splitting efficiencies of  $BaTaO_2N$  have been progressively improved, it is still far from the requirements set for practical applications. Therefore, various promising strategies have been developed to improve the photocatalytic and photoelectrochemical water splitting efficiencies of  $BaTaO_2N$ , including creating a solid-solution,

developing a new synthesis approach, reducing the defect density, selecting appropriate oxide precursors, controlling the exposed surface, engineering an effective cocatalyst, etc. For instance, Maeda and Domen<sup>16</sup> achieved the solar water splitting to produce H<sub>2</sub> and O<sub>2</sub> above 660 nm using a BaZrO<sub>3</sub>-BaTaO<sub>2</sub>N solid solution as an anode material in a photoelectrochemical cell with an external bias of 1.0 V (vs. Pt). BaTaO<sub>2</sub>N synthesized from the nitridation of (Na<sub>1/4</sub>Ba<sub>3/4</sub>)(Zn<sub>1/4</sub>Ta<sub>3/4</sub>)O<sub>3</sub> exhibited an enhanced oxygen evolution activity with an apparent quantum yield of 11.9% at 420 nm.<sup>17</sup> A one-step NH<sub>3</sub>-assisted flux growth method was demonstrated to enhance the water-splitting activity of BaTaO<sub>2</sub>N via reducing the defect density, which is generally resulted from a long high-temperature nitridation.<sup>18,19</sup> Recent studies on the effect of different exposed surfaces found that the BaTaO<sub>2</sub>N crystals with well-developed {111} facets<sup>20</sup> and co-exposed {100} and {110} facets<sup>21</sup> can exhibit a significantly enhanced photocatalytic activity for H<sub>2</sub> evolution in comparison to the BaTaO<sub>2</sub>N with only {100} facets. Very recently, the sequential decoration of Pt cocatalyst on RbCl-flux-grown BaTaO<sub>2</sub>N particulates by impregnation-reduction followed by a site-selective photodeposition led to over 100 times more efficient H<sub>2</sub> evolution than before, with an apparent quantum yield of 6.8% at 420 nm, and a solar-to-hydrogen energy conversion efficiency of 0.24% in Z-scheme water splitting.<sup>22</sup>

One of the effective strategies to enhance the water-splitting efficiency is modifying the physicochemical and photophysical properties by an intentional introduction of foreign cations with different radii and valences into the *A*-site and/or *B*-site of AB(O,N)<sub>3</sub> and ABO<sub>3</sub> perovskite hosts. In this way, the band-edge position, optical absorption, charge density, charge mobility, charge separation, electrical conductivity, defect density, etc. can be modified to combat low water-splitting efficiency.<sup>23</sup> The SrCl<sub>2</sub> flux-mediated Al doping in SrTiO<sub>3</sub> resulted in an apparent quantum efficiency of 30% at 360 nm in the overall water splitting reaction.<sup>24</sup> Recently, Mg-modified BaTaO<sub>2</sub>N exhibited an apparent quantum efficiency as high as 2.59% at 420±20 nm due to the stronger Ta–O/N bonds, lower concentration of Ta<sup>4+</sup> defects, and positive shift of band-edge positions.<sup>25</sup> The partial substitution of Ta<sup>5+</sup> cations in BaTaO<sub>2</sub>N by higher valent Mo<sup>6+</sup> was found to increase the donor density effectively, enhancing the photoelectrochemical water splitting under visible light irradiation.<sup>26</sup> On

the other hand, doping of a lower-valent cation to intentionally introduce oxygen vacancies and decrease  $\text{Ti}^{3+}$ -related defects was effective to enhance the photocatalytic activity of  $\text{SrTiO}_3$  for water splitting.<sup>27</sup>

In this context, we demonstrate the effect of *B*-site doping of select aliovalent metal cations of lower valency on enhancing the sacrificial photocatalytic  $\text{H}_2$  and  $\text{O}_2$  evolution of  $\text{BaTaO}_2\text{N}$  (BTON) under visible light irradiation. Particularly, the present study emphasizes on the elucidation of the respective physicochemical correlation between the photocatalytic  $\text{H}_2$  and  $\text{O}_2$  evolution reaction rates and adsorption energy of intermediates (obtained from molecular dynamics simulations) for BTON:Al, BTON:Ga, BTON:Mg, BTON:Sc, and BTON:Zr photocatalysts synthesized by the flux method. Therefore, the rationalization of the experimental kinetics data is provided through the adsorption energy-performance plots, which has not been reported previously for the BTON-based photocatalysts. In fact, this highlights the important role of surface properties in complex photocatalytic systems. Specifically, the influence of divalent ( $\text{Mg}^{2+}$ ), trivalent ( $\text{Al}^{3+}$ ,  $\text{Ga}^{3+}$ , and  $\text{Sc}^{3+}$ ), and tetravalent ( $\text{Zr}^{4+}$ ) cations on optoelectronic properties, adsorption energy of chemical species ( $\text{H}_2\text{O}$ ,  $\text{H}^+$ ,  $\text{H}^*$ , and  $\text{H}_2$  for HER and  $\text{H}_2\text{O}$ ,  $\text{HO}^*$ ,  $\text{O}^*$ ,  $\text{HOO}^*$ , and  $\text{O}_2$  for OER), and sacrificial photocatalytic  $\text{H}_2$  and  $\text{O}_2$  evolution on  $\text{BaTaO}_2\text{N}$  is studied.

## 2. EXPERIMENTAL

### 2.1. Synthesis

Pristine and cation-doped  $\text{BaTaO}_2\text{N}$  photocatalysts were synthesized by a flux-mediated ammonolysis method. All reagents used in this study were purchased from FUJIFILM Wako Pure Chemical Corporation. Reagent-grade  $\text{BaCO}_3$  (99.9%) and  $\text{Ta}_2\text{O}_5$  (99.9%) were employed as solute, and KCl (99.5%) was used as flux.  $\text{Al}_2\text{O}_3$ ,  $\text{Ga}_2\text{O}_3$ ,  $\text{MgO}$ ,  $\text{Sc}_2\text{O}_3$ , and  $\text{ZrO}_2$  (>99%) were used as dopant sources. Solute with a concentration of 50 mol%, flux, and dopant (5%) source were dry mixed manually in a stoichiometric ratio (Table S1) for 30 min using an agate mortar and a pestle. The well-homogenized mixture was transferred into a platinum crucible ( $4.0\text{ cm}^3$ ), heated at  $900^\circ\text{C}$  for  $7\text{ h} \times 2$  times, with an intermediate mixing with the KCl flux between heating, at a heating rate of  $600^\circ\text{C}\cdot\text{h}^{-1}$  under an  $\text{NH}_3$  flow ( $200\text{ mL}\cdot\text{min}^{-1}$ ), and cooled naturally. The resulting powder samples were

collected, washed with dilute HNO<sub>3</sub> and deionized water repeatedly, and dried at 100°C for 12 h. According to the dopant type, the BaTaO<sub>2</sub>N photocatalysts were denoted as BTON, BTON:Al, BTON:Ga, BTON:Mg, BTON:Sc, and BTON:Zr.

## 2.2. Characterization

The X-ray diffraction (XRD) patterns were acquired with a MiniflexII (Rigaku) diffractometer using Cu-K $\alpha$  radiation ( $\lambda = 0.15418$  nm) in the  $2\theta$  scan range from 5° to 80° and compared with entries from the ICDD-PDF-2 powder diffraction pattern database. The nano- and microstructures of the samples were observed using an ARM-200FC transmission electron microscope (JEOL) and a JSM-7600F field-emission-type scanning electron microscope (JEOL) equipped with energy-dispersive X-ray spectroscopy, respectively. The UV-Vis diffuse reflectance spectra were measured on a UV-3600 UV-Vis-NIR spectrophotometer (Shimadzu). The measured reflectance spectra were then converted to the Kubelka-Munk function, and the bandgap values were estimated using the Tauc plots.<sup>28</sup> The surface chemical compositions and chemical states were analyzed by means of X-ray photoelectron spectroscopy (JPS-9010MC, JEOL) with nonmonochromated Mg-K $\alpha$  radiation (1253.6 eV). The details of density functional theory (DFT) calculations and transient absorption spectroscopy (TAS) measurements are given in Supporting Information.

## 2.3. Photocatalytic H<sub>2</sub> and O<sub>2</sub> evolution tests

The photocatalytic H<sub>2</sub> and O<sub>2</sub> evolution half-reactions were separately carried out in a Pyrex<sup>®</sup> side-irradiation-type reaction vessel connected to a gas-closed-circulation system equipped with a gas chromatograph (GC-8A, TCD, Shimadzu) and a vacuum pump. A 300 W Xe arc lamp (Cermax-PE300BF, PerkinElmer) with a UV-cutoff filter (L42, HOYA) and a cold mirror (CM-1, Optline) was employed as a visible-light source, and the irradiance of visible light was 200 mW·cm<sup>-2</sup>. For O<sub>2</sub> evolution, 100 mg of CoO<sub>x</sub>-loaded photocatalyst, 300 mL of 10 mM AgNO<sub>3</sub> (sacrificial electron scavenger), and 200 mg of La<sub>2</sub>O<sub>3</sub> (pH buffer) were used, while 100 mg of Pt-loaded photocatalyst and 300 mL of 10 vol% aqueous methanol solution were employed for H<sub>2</sub> evolution. Pristine and cation-doped BaTaO<sub>2</sub>N photocatalysts were loaded with CoO<sub>x</sub> (2 wt% Co) and Pt (0.5 wt%) nanoparticles as O<sub>2</sub> and H<sub>2</sub> evolution cocatalysts by impregnation in aqueous solutions of

$\text{Co}(\text{NO}_3)_2 \cdot 6\text{H}_2\text{O}$  (>99.5%, FUJIFILM Wako Pure Chemical Corporation) and  $\text{H}_2\text{PtCl}_6 \cdot 2\text{H}_2\text{O}$  (Kanto Chemicals, 97% Pt), followed by heating at 700°C for 1 h under an  $\text{NH}_3$  flow (200  $\text{mL} \cdot \text{min}^{-1}$ ) and re-oxidizing at 200°C for 1 h in air and at 200°C for 1 h under  $\text{H}_2$  atmosphere, respectively.

## 2.4. Molecular modeling of adsorption

Molecular dynamics (MD) simulations were applied to estimate potential energy for the adsorption of water and methanol molecules onto the predominant (110) surface of pristine and cation-doped  $\text{BaTaO}_2\text{N}$ .<sup>29-31</sup> The adsorption energy of the interactions of water and methanol molecules on the predominant (110) surface of pristine and cation-doped  $\text{BaTaO}_2\text{N}$  was calculated by Forcite and Adsorption Locator modules in BIOVIA Materials Studio 2017 software. The simulations were performed with a slab thickness of 5 Å, a supercell of  $4 \times 6$ , and a vacuum of 20 Å along the  $c$  axis in the simulation box with a size of  $(16.45 \times 23.26 \times 34.54) \text{ Å}^3$  in periodic boundary conditions to exclude arbitrary boundary effect. Adsorption on the exposed surfaces with different terminations was studied in the following assumptions: (i) the adsorption surface mainly contains the  $\text{TaO}_6$  octahedra, (ii) the adsorption surface mainly contains the  $\text{TaN}_6$  octahedra, and (iii) the adsorption surface mainly contains the  $\text{Ta}_2\text{N}_2\text{O}_4$  octahedra. During the MD simulations, the adsorption-desorption equilibria and effects of different chemical species ( $\text{H}_2\text{O}$ ,  $\text{H}^+$ ,  $\text{H}^*$ , and  $\text{H}_2$  for HER and  $\text{H}_2\text{O}$ ,  $\text{HO}^*$ ,  $\text{O}^*$ ,  $\text{HOO}^*$ , and  $\text{O}_2$  for OER) were also taken into consideration to understand the relationship between the adsorption and photocatalytic activity of pristine and cation-doped  $\text{BaTaO}_2\text{N}$ .

## 3. RESULTS AND DISCUSSION

The XRD patterns of pristine and cation-doped  $\text{BaTaO}_2\text{N}$  photocatalysts are shown in Figure 1a. All samples have identical reflections assignable to the perovskite phase  $\text{BaTaO}_2\text{N}$  with cubic structure with space group  $Pm\bar{3}m$  (ICDD PDF 01-084-1748). The absence of emerging reflections attributable to the foreign crystalline phases indicates that pristine and cation-doped  $\text{BaTaO}_2\text{N}$  photocatalysts with high phase-purity can be successfully synthesized by applying current synthesis conditions. Figure 1b shows the enlarged XRD patterns indicating the change in the  $2\theta$  angle position of the (110) reflection. A slight shift of reflections towards a higher  $2\theta$  angle is noted when  $\text{Ta}^{5+}$  is partially substituted by  $\text{Al}^{3+}$  (53.5 pm) or  $\text{Ga}^{3+}$  (62 pm) in the octahedral coordination, suggesting the lattice



volume contraction due to the introduction of dopants with smaller ionic radii (Figures 1b and 1c). Also, a slight shift of reflections towards a lower  $2\theta$  angle is observed when  $\text{Ta}^{5+}$  (64 pm) is partially substituted by  $\text{Mg}^{2+}$  (72 pm),  $\text{Sc}^{3+}$  (74.5 pm) or  $\text{Zr}^{4+}$  (72 pm) in the octahedral coordination, indicating the lattice volume expansion due to the incorporation of dopants with larger ionic radii (Figures 1d-f). On the contrary, the cosubstitution of  $\text{Mg}^{2+}$  and  $\text{Zr}^{4+}$  for  $\text{Ta}^{5+}$  in  $\text{Ta}_3\text{N}_5$  was followed by the  $\text{O}^{2-}$ -to- $\text{N}^{3-}$  substitution to compensate the imbalance of ionic charge, and the concurrent substitution of  $\text{O}^{2-}$  for  $\text{N}^{3-}$  reduced the extent of lattice expansion.<sup>32</sup> Since the content of aliovalent metal cations replacing the  $\text{Ta}^{5+}$  partially in the octahedral coordination is limited to 5%, small octahedral tilting and structural distortion as well as change in the O:N ratio are expected, which can influence the band structure, band gap, light absorption, and photocatalytic activity.

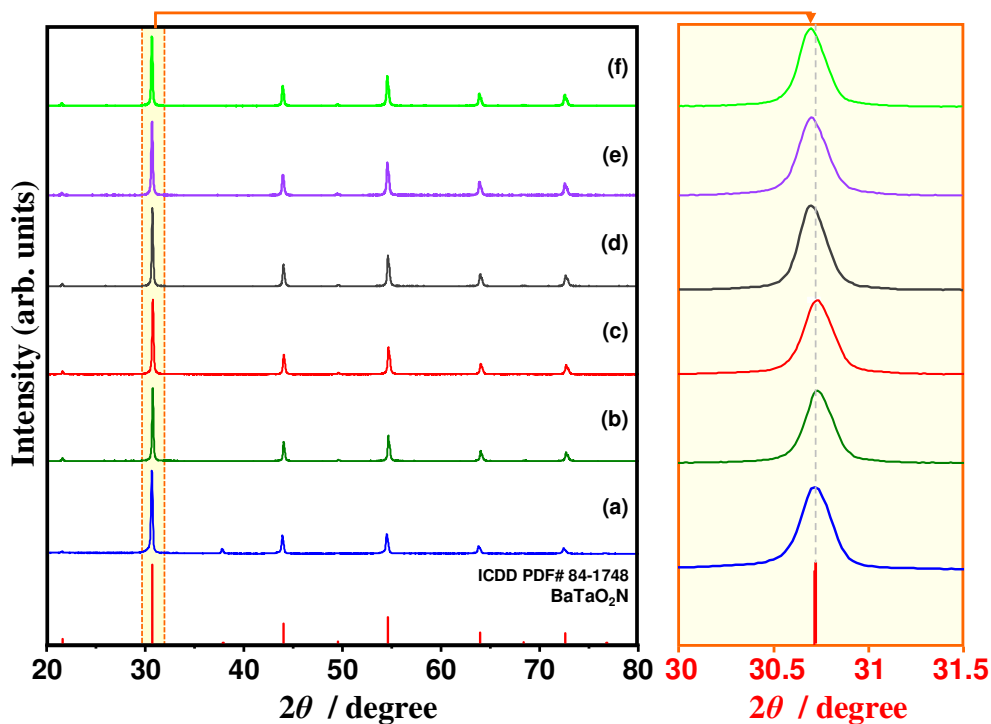


**Figure 1.** XRD patterns of BTiO<sub>2</sub>N (a), BTiO<sub>2</sub>N:Al (b), BTiO<sub>2</sub>N:Ga (c), BTiO<sub>2</sub>N:Mg (d), BTiO<sub>2</sub>N:Sc (e), and BTiO<sub>2</sub>N:Zr (f).

The effect of doping on overall morphology and particle size of BaTaO<sub>2</sub>N photocatalysts was examined by scanning electron microscopy (SEM). Figure 2 shows the SEM images and corresponding particle-size distribution histograms of pristine and cation-doped BaTaO<sub>2</sub>N

photocatalysts. As shown, the BTON, BTON:Al, BTON:Ga, BTON:Sc, and BTON:Zr photocatalysts have a similar morphology, where the plate-like submicron-sized structures dominate over other structures having an idiomorphic shape with well-developed crystal facets. Two-dimensional plate-like structures are known to provide a short bulk-to-surface travel distance for photogenerated charge carriers, suppressing the recombination, and a large section area for obtaining a sufficient photon flux density, promoting the charge separation and transfer for efficient photocatalytic reactions.<sup>33</sup> Due to its cubic crystal structure, BaTaO<sub>2</sub>N commonly crystallizes into a cubic shape even when Ba<sub>5</sub>Ta<sub>4</sub>O<sub>15</sub> with plate-like structures is involved as an intermediate phase.<sup>18</sup> Nevertheless, because of a small lattice mismatch (0.7%) in the atomic arrangements of the Ba<sub>5</sub>Ta<sub>4</sub>O<sub>15</sub> (001) plane and the BaTaO<sub>2</sub>N (111) plane,<sup>20</sup> plate-like submicron-sized structures of BaTaO<sub>2</sub>N were successfully synthesized under current synthesis conditions, which are advantageous for improving the photocatalytic performance for H<sub>2</sub> and O<sub>2</sub> evolution. Similarly, Luo et al.<sup>20</sup> have also synthesized platy BaTaO<sub>2</sub>N crystals with well-developed {111} facets via the simultaneous formation and transformation of Ba<sub>5</sub>Ta<sub>4</sub>O<sub>15</sub> using K<sub>2</sub>CO<sub>3</sub>/KCl binary flux and achieved an excellent photocatalytic performance for H<sub>2</sub> evolution. In contrast, the number of plate-like structures is significantly reduced, and irregular structures with idiomorphic shape become prevailing in the BTON:Mg. This implies that the Mg<sup>2+</sup> dopant tends to influence the total interfacial free energy and kinetic factors stronger than other dopants. The BTON has an average particle size of 47 nm, which is increased to 162, 165, 127, 163, and 164 nm by introducing the Al<sup>3+</sup>, Ga<sup>3+</sup>, Mg<sup>2+</sup>, Sc<sup>3+</sup>, and Zr<sup>4+</sup> dopants, respectively, indicating the crystal growth promoted by dopants. The bright-field transmission electron microscopy (TEM) images of pristine and cation-doped BaTaO<sub>2</sub>N photocatalysts in Figure S1 also confirm the existence of plate-like submicron-sized structures along with idiomorphic crystals. The high-resolution TEM (HRTEM) images show a 0.29-nm spacing between the parallelly adjacent lattice fringes, which agrees well with the {110} lattice spacing of BaTaO<sub>2</sub>N, and no clear defects in the analyzed area of the crystallite are noted, corroborating their high crystallinity. Irregular diffraction spots observed in the selected area electron diffraction (SAED) patterns are indexed to the (110), (200), (211), and (220) planes of cubic BaTaO<sub>2</sub>N, revealing the randomly oriented nature of crystallites.

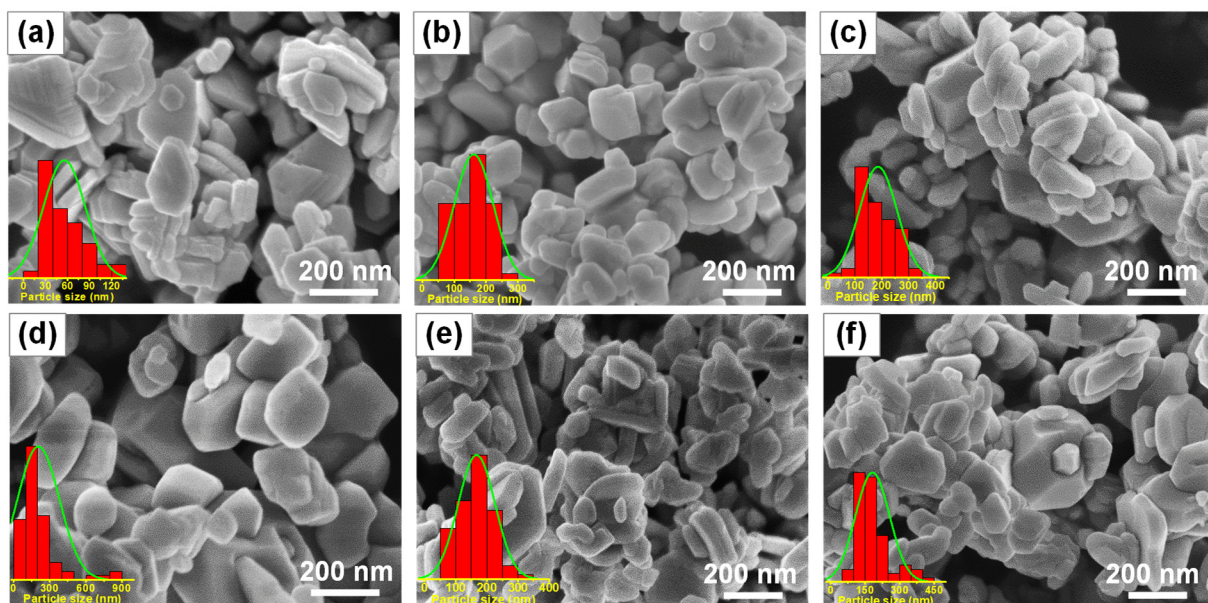


**Figure 2.** SEM images of BTON (a), BTON:Al (b), BTON:Ga (c), BTON:Mg (d), BTON:Sc (e), and BTON:Zr (f).

Figure 3 shows the UV-Vis diffuse reflectance spectra of pristine and cation-doped BaTaO<sub>2</sub>N photocatalysts. The BTON shows an absorption edge at 665 nm, corresponding to the band gap of 1.86 eV. The UV-Vis diffuse reflectance spectra of cation-doped BTON photocatalysts resemble that of BTON, showing a steep onset in light absorption at about 665 nm with a mild change. Accordingly, a slight change in the bandgap energy value, which was estimated by extrapolating the straight-line portion of the absorption spectra to zero absorbance, is observed for BTON:Al (1.84 eV), BTON:Ga (1.85 eV), BTON:Mg (1.91 eV), BTON:Sc (1.86 eV), and BTON:Zr (1.89 eV) photocatalysts. It can be noted in Figure 3 that only the BTON:Mg photocatalyst possesses the brightest reddish-brown color compared to other BTON photocatalysts with a slightly darker reddish-brown color and shows a sub-band gap absorption beyond the absorption edge due possibly to the presence of anion vacancy or variation in the O:N ratio. In general, the bandgap enlargement/diminution is observed by the tilting of the octahedra stemming from the insertion of cations with different sizes.<sup>34</sup> Such pronounced trend is not observed here because the changes in the structural distortion and octahedral tilting are relatively insignificant due to a small amount of dopant used and less bond angle variations.<sup>35,36</sup>

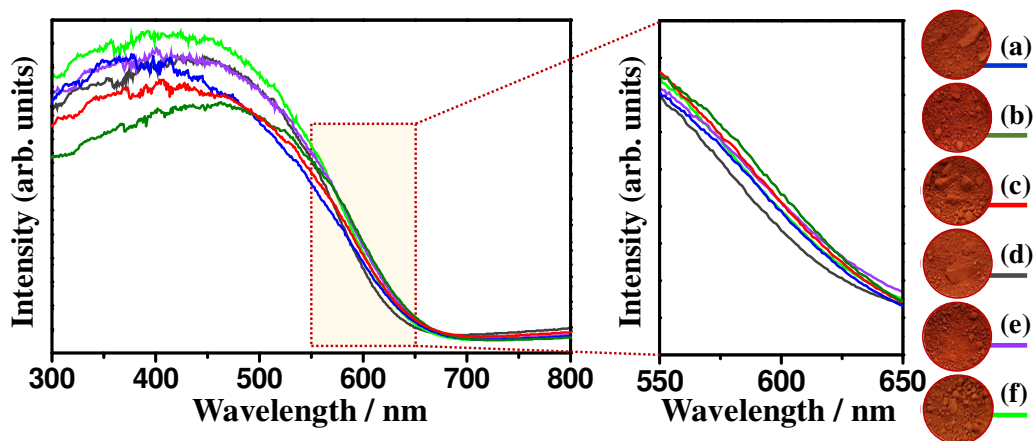


**Figure 3.** UV-Vis diffuse reflectance spectra and digital photographs of BTON (a), BTON:Al (b), BTON:Ga (c), BTON:Mg (d), BTON:Sc (e), and BTON:Zr (f).

The XPS survey spectra in Figure S2 confirm the presence of Ba, Ta, O, N, Al, Ga, Mg, Sc, Zr, and adventitious carbon in pristine and cation-doped BaTaO<sub>2</sub>N photocatalysts. The amount of dopant and O:N ratio estimated by EDS and XPS analyses are 0% and 2.27 for BTON, 5.2% Al and 2.17 for BTON:Al, 4.8% Ga and 2.08 for BTON:Ga, 5.1% Mg and 2.50 for BTON:Mg, 4.7% Sc and 2.13 for BTON:Sc, and 4.9% Zr and 2.32 for BTON:Zr, respectively. The XPS valence band (VB) spectra were measured for all photocatalysts after Ar etching to remove surface defects and Pt coating to mitigate surface charge effect. As shown in Figure S3, the XPS-VB spectra corrected using the C 1s peak shifts show the relative positions of the valence band maximum edges of BTON, BTON:Al, BTON:Ga, BTON:Mg, BTON:Sc, and BTON:Zr at 1.74, 1.60, 1.50, 1.67, 1.37, and 1.77 eV, respectively. Knowing that  $E_g = E_{VB} - E_{CB}$ , the relative positions of the corresponding conduction bands ( $E_{CB}$ ) were estimated, using the bandgap values ( $E_g$ ) measured experimentally by ultraviolet-visible spectroscopy and the relative positions of the valence bands ( $E_{VB}$ ) analyzed by X-ray photoelectron spectroscopy, to be -0.12, -0.24, -0.35, -0.24, -0.49, and -0.12 eV for BTON, BTON:Al, BTON:Ga, BTON:Mg, BTON:Sc, and BTON:Zr, respectively (Figure S4). The conduction bands in oxynitride compounds are dominated by the Ta 5d orbitals, while the valence bands are determined by the O 2p and N 2p orbitals with a strong dependence on the energy of the N 2p states.<sup>37</sup> In addition, for *n*-type semiconductors, the Fermi level is close to the potential of the conduction band. According to the  $E_{CB}$  values estimated for pristine and cation-doped BTON photocatalysts, it should be noted

that the modification of BaTaO<sub>2</sub>N with divalent (Mg<sup>2+</sup>) and trivalent (Al<sup>3+</sup>, Ga<sup>3+</sup> and Sc<sup>3+</sup>) cations shifts the respective  $E_{CB}$  to more negative values, which is consistent with the partial modification by substitution for Ta<sup>5+</sup>. In contrast, modification with a tetravalent cation (Zr<sup>4+</sup>) does not change the  $E_{CB}$  value compared to that obtained for pristine BTON presumably due to the compensation provided by the change of  $E_{VB}$  to more positive values. This is possible if it is considered that the incorporation of a dopant with higher ionic radii (Zr<sup>4+</sup>) leads to a greater substitution of O<sup>2-</sup> for N<sup>3-</sup> to compensate the ionic charge imbalance<sup>32</sup>, justifying the change in the  $E_{VB}$  in the BTON:Zr.

The effect of the *B*-site-selective doping of aliovalent metal cations on sacrificial visible-light-induced photocatalytic O<sub>2</sub> and H<sub>2</sub> evolution was studied. Figure 4 shows the half-reaction time courses for the photocatalytic O<sub>2</sub> and H<sub>2</sub> evolution over pristine and cation-doped BaTaO<sub>2</sub>N photocatalysts loaded with CoO<sub>x</sub> and Pt cocatalysts, respectively. The total amount of evolved O<sub>2</sub> reached 503.6, 446.8, 416.2, 316.3, 252.5, and 188.0 μmol for BTON:Mg, BTON:Zr, BTON:Sc, BTON, BTON:Ga, and BTON:Al within 5 h, respectively. This implies that the Mg<sup>2+</sup>, Sc<sup>3+</sup>, and Zr<sup>4+</sup> dopants had a positive effect on improving the photocatalytic O<sub>2</sub> evolution, while the Al<sup>3+</sup> and Ga<sup>3+</sup> dopants influenced negatively. In contrast, the BTON showed the lowest H<sub>2</sub> evolution (30.5 μmol) within 5 h, which was increased to 50.1, 56.7, 61.8, 80.4, and 117.4 μmol by doping with Ga<sup>3+</sup>, Mg<sup>2+</sup>, Sc<sup>3+</sup>, Zr<sup>4+</sup>, and Al<sup>3+</sup>. Although the BTON:Mg and BTON:Al independently exhibited the highest amounts of evolved O<sub>2</sub> (503.6 μmol) and H<sub>2</sub> (117.4 μmol) among the synthesized BTON photocatalysts, respectively, the BTON:Zr showed the high photocatalytic activities in both O<sub>2</sub> (446.8 μmol) and H<sub>2</sub> (80.4 μmol) evolution reactions. Since there is no large difference in crystal structure, particle size, particle morphology, and light absorption, the varying amounts of O<sub>2</sub> and H<sub>2</sub> evolved during the photocatalytic half-reactions over pristine and cation-doped BaTaO<sub>2</sub>N photocatalysts can be interpreted by involving the optical, electronic, and surface properties.

Kisch and Bahnemann<sup>38</sup> stated that for the photocatalytic systems based on suspensions of semiconductor particles in dissolved substrates, the reaction rates are suitable for comparison. In fact, rates must be measured with the same type of photoreactor under identical irradiation conditions, and it is important that the intensity of the incident light is integrated in the same wavelength range. The

following reaction rates were estimated for pristine and cation-doped BaTaO<sub>2</sub>N photocatalysts: 6.59, 21.92, 10.27, 11.59, 12.12, and 16.44  $\mu\text{mol H}_2\cdot\text{h}^{-1}$  for BTON, BTON:Al, BTON:Ga, BTON:Mg, BTON:Sc, and BTON:Zr at AM1.5 G illumination ( $200\text{ mW}\cdot\text{cm}^{-2}$ ), respectively, indicating that the higher H<sub>2</sub> evolution rate was achieved using Al dopant. Maeda and Domen<sup>16</sup> reported a 14.1  $\mu\text{mol H}_2\cdot\text{h}^{-1}$  rate using the BaZrO<sub>3</sub>-BaTaO<sub>2</sub>N (Zr/Ta=0.05) solid-solution photocatalyst under AM1.5 G illumination using methanol as sacrificial reagent. Using the same photocatalytic reaction system, Domen and coworkers<sup>22</sup> achieved an apparent quantum yield (AQY) of 6.8% at 420 nm for BaTaO<sub>2</sub>N photocatalyst with an optimized cocatalyst decoration, which generated about 220  $\mu\text{mol H}_2\cdot\text{h}^{-1}$  under AM1.5 G illumination. The reaction rates of O<sub>2</sub> and H<sub>2</sub> evolution over pristine and cation-doped BaTaO<sub>2</sub>N photocatalysts are tabulated in Table S2 in Supporting Information.

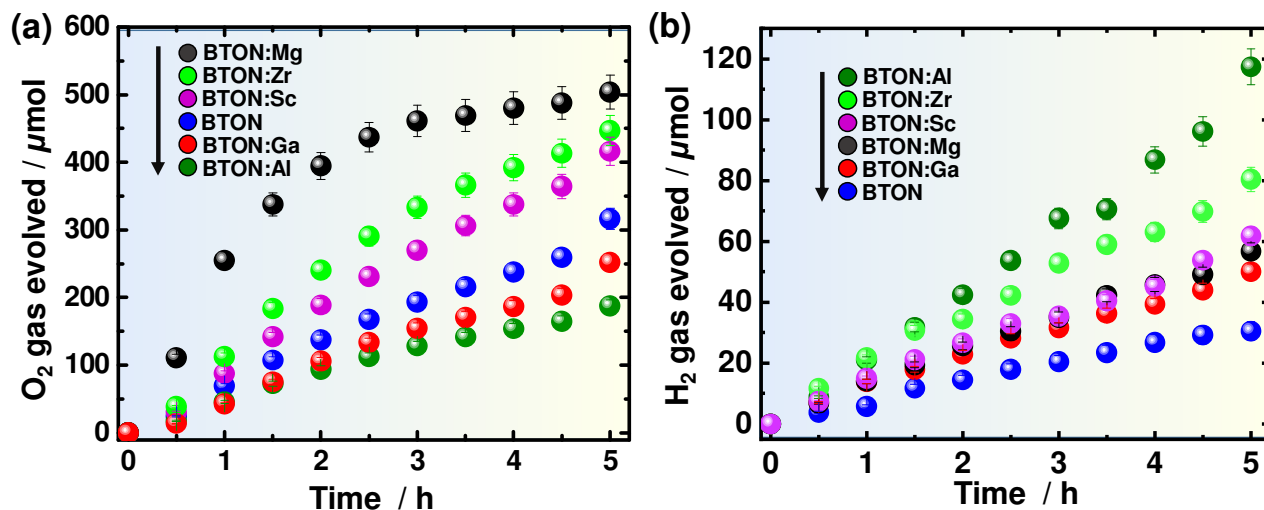


**Figure 4.** Reaction time courses for photocatalytic O<sub>2</sub> (a) and H<sub>2</sub> (b) evolution over BTON, BTON:Al, BTON:Ga, BTON:Mg, BTON:Sc, and BTON:Zr. For photocatalytic O<sub>2</sub> evolution reaction, 100 mg photocatalyst loaded with CoO<sub>x</sub> cocatalyst (2 wt% Co), aqueous solution of AgNO<sub>3</sub> (10 mM, 300 mL), and 200 mg La<sub>2</sub>O<sub>3</sub> (pH buffer) were used. For photocatalytic H<sub>2</sub> evolution reaction, 100 mg photocatalyst loaded with Pt cocatalyst (0.5 wt%) and aqueous solution of methanol (10 vol%, 300 mL) were used. Light source was 300 W Xe lamp fitted with a cutoff filter ( $\lambda > 420\text{ nm}$ ) and a cold mirror (CM-1), and a side-irradiation-type reaction vessel was used in this study.

Exploring the linkage of the photocatalytic activities of pristine and cation-doped BaTaO<sub>2</sub>N photocatalysts with the optical, electronic, and surface properties allows to gain insights into the effect of the factors governing the photocatalytic O<sub>2</sub> and H<sub>2</sub> evolution.<sup>31,39</sup> Considering the UV-Vis diffuse reflectance spectra of pristine and cation-doped BaTaO<sub>2</sub>N photocatalysts, presumably there is an

increase in the density of holes with cation doping in our study.<sup>40</sup> As mentioned earlier, the bandgap values vary slightly upon cation doping, indicating only the ability of the photocatalysts to absorb a large proportion of visible light (<665 nm). The results from DFT-HSE12s calculations (Supporting Information) reveal that the *p*-type doping of aliovalent cations reduces the bandgap value possibly due to the formation of defects and the shift of the top of the valence band toward the conduction band and vice versa (Figure S5), allowing more visible-light photons to be involved in the photocatalytic reactions. Apparently, the *p*-type doping of BaTaO<sub>2</sub>N causes the shift of the Fermi level due to the lack of electrons in the cation-doped BaTaO<sub>2</sub>N photocatalysts because the charge balance is not compensated<sup>41,42</sup> in comparison to the charge compensated models.<sup>43</sup> The direct-type transition of BaTaO<sub>2</sub>N was retained when doped with aliovalent cations. The DOS plots in Figure S6 confirm that the valence band predominantly consists of O *p* and N *p* states and the conduction band contains Ta *d* states. Although 12.5 at% dopant was involved during *ab initio* modeling, the distribution pattern of the electronic states remains primarily unchanged, and the other electron states are insignificant. In all cases, the relative change in the population of electronic states with the modification by cation doping supports the possibility that there are differences in the density of the charge carriers of pristine and cation-doped BaTaO<sub>2</sub>N photocatalysts when irradiated.

In fact, it was previously reported that the co-doping of BaTaO<sub>2</sub>N with Mg and Zr could result in the generation of high population of long-lived electrons, altering the charge-transfer properties and enhancing the photocatalytic activity.<sup>40</sup> Then, it is argued that under the same visible light irradiation, the density of holes increases due to the *p*-type doping.<sup>26</sup> The higher density of holes is expected to promote the charge transfer and to increase the lifetime,<sup>40</sup> enhancing the O<sub>2</sub> and H<sub>2</sub> evolution over BTON:Mg and BTON:Zr, respectively. In fact, the results of transient absorption spectroscopy (TAS) measurement confirm that the photocarrier lifetime is increased by cation doping (Figures 5a, 5b, and S7). For H<sub>2</sub> evolution, all cation-doped photocatalysts exhibited a significant improvement in relation to pristine BTON. However, for O<sub>2</sub> evolution, doping the BTON with Al<sup>3+</sup> and Ga<sup>3+</sup> resulted in lower yields. Previously, the doping effects of Al<sup>3+</sup> and Ga<sup>3+</sup> on various photocatalysts have been reported to change the density of charge carriers.<sup>24,44,45</sup> Among many factors, the adsorption energies of

intermediates play an important role during the oxidation of water,<sup>31</sup> which can be relevant to explain the kinetic effect observed in the photocatalytic O<sub>2</sub> evolution over BTON:Al and BTON:Ga (discussed later).

The effect of surface doping of Ta<sub>3</sub>N<sub>5</sub> with Mg and Zr in relation to the electronic properties was studied by Seo et al.<sup>32</sup> and Wang et al.<sup>46</sup>, and similar reports were made for cation-doped BaTaO<sub>2</sub>N surfaces.<sup>25,26</sup> Figure S4 shows the potentials of the valence and conduction bands of pristine and cation-doped BaTaO<sub>2</sub>N photocatalysts synthesized in the present study. Both values of cation-doped BaTaO<sub>2</sub>N photocatalysts became slightly more negative compared to those of pristine BTON. Presumably, changing these potentials affected the tendency of the electron transfer.<sup>32</sup> As an example, an efficient electron transfer in the BaTaO<sub>2</sub>N photocatalysts was previously achieved by increasing the photocurrent and lower-onset-potential significantly for water oxidation.<sup>12,15,32</sup> The change in the potential values of the valence and conduction bands is a manifestation of the variation of electronic properties that can control the dynamics and transfer of photogenerated charge carriers at the semiconductor-electrolyte interface. Particularly, in the case of Ta<sub>3</sub>N<sub>5</sub> modified with Mg and Zr, the potential values of the valence and conduction bands became more negative compared to pristine Ta<sub>3</sub>N<sub>5</sub>.<sup>32</sup> In addition, doping with Mg<sup>2+</sup> could also alter the decay of the open circuit potential by interrupting the irradiation of light, leading to the changes in the lifetimes of charge carriers.<sup>25</sup> This change is also related to the appearance of mid-gap states associated with the formation of anion defects stemming from the doping of a cation with lower valence.<sup>25,27,46,47</sup> Furthermore, small ionic radii induce a greater distortion of octahedra, resulting in a narrow conduction band, and the longer the Ta–O/N bond distances, the conduction band minimum becomes antibonding.<sup>34</sup> Therefore, the higher H<sub>2</sub> evolution over BTON:Al can be justified by the reduction reaction in the conduction band of BTON:Al due to the slowed recombination rate of photogenerated charge carriers.<sup>26</sup> The fact that the host cation induces a decrease in the recombination process,<sup>26,47</sup> allowing to qualitatively understand the trends in the photocatalytic O<sub>2</sub> and H<sub>2</sub> evolution over cation-doped BaTaO<sub>2</sub>N photocatalysts. In all cases, the change in the band structures leads to the valence and conduction



bands to have thermodynamically sufficient overpotentials for the oxidation and reduction of water (Figure S4).

The photocatalytic activity of photocatalysts also depends on their surface properties. Recent studies<sup>25,48</sup> demonstrated the effects of cation doping and the generation of defects in BaTaO<sub>2</sub>N. Particularly, the surface properties of photocatalysts reveal how the chemical reactions proceed and how the interactions between the intermediates and the photocatalyst surface occur. Finding the adsorption energy - performance relationships in photocatalysis is important for understanding the reaction kinetics and targeting the requirements set for practical applications.<sup>40</sup> For that, the adsorption energies of intermediates are first estimated theoretically and then correlated with the experimental reaction rates of H<sub>2</sub> and O<sub>2</sub> evolution. It is well documented that in the case of H<sub>2</sub> evolution, the key intermediate is adsorbed H\*, and the intermediates that form during the water oxidation are HO\*, O\*, and HOO\*.<sup>48,49</sup> The role of the surface properties on enhancing the photocatalytic O<sub>2</sub> and H<sub>2</sub> evolution over pristine and cation-doped BaTaO<sub>2</sub>N photocatalysts is discussed in the following section.

The interaction between water molecules and the photocatalyst surface is one of the key factors affecting directly the reaction pathways of photocatalytic water splitting. Therefore, the interfacial adsorption configuration of water molecules has been studied using various computational methods. For instance, in a single g-C<sub>3</sub>N<sub>4</sub> sheet, water molecules can be adsorbed around the intrinsic vacancy at the low coverage of water, whereas the hydrogen bonds between water molecules can assist stabilizing the water adsorption at the high coverage of water, leading to the reduction of the valence and conduction bands.<sup>50</sup> However, controversies over the modes of the interaction of water molecules on the surfaces of materials and intermediates during the photocatalytic reactions are still being explored in the field of photocatalysis using different computational methods, including density functional theory (DFT).<sup>49,51-54</sup>

Here, we applied molecular dynamics (MD) calculations to theoretically explore the interactions of water and methanol molecules with the predominant (110) surfaces, terminated with TaO<sub>6</sub>, TaN<sub>6</sub>, and TaO<sub>4</sub>N<sub>2</sub> octahedra, of BTON, BTON:Al, BTON:Ga, BTON:Mg, BTON:Sc, and BTON:Zr using a

field density distribution and close contacts (a scaled sum of van der Waals radii). Table S3 shows the adsorption energy values obtained by MD calculations. Figures S8-S10 show that on the TaO<sub>6</sub>-, TaN<sub>6</sub>, and TaO<sub>4</sub>N<sub>2</sub>-terminated (110) surfaces, water molecules can be adsorbed in a similar way by forming the clusters around the atoms. On the TaO<sub>6</sub>-terminated (110) surfaces, close contacts only in BTON:Mg and high affinity of methanol molecules in BTON:Al and BTON:Zr are observed, while close contacts in BTON:Mg, BTON:Sc, and BTON:Zr and high affinity of methanol molecules in BTON:Al, BTON:Ga, and BTON:Zr are noted on the TaN<sub>6</sub>-terminated (110) surfaces. On the TaO<sub>4</sub>N<sub>2</sub>-terminated (110) surfaces, close contacts in BTON:Mg, BTON:Sc, and BTON:Zr and high affinity of methanol molecules in BTON:Sc and BTON:Zr are remarked. In all TaO<sub>6</sub>-, TaN<sub>6</sub>-, and TaO<sub>4</sub>N<sub>2</sub>-terminated (110) surfaces, the BTON:Mg and BTON:Zr show a higher number of close contacts, whereas the BTON:Al and BTON:Zr show a high affinity to methanol molecules. As an example, the close contacts of the TaO<sub>4</sub>N<sub>2</sub>-terminated (110) surfaces of BTON, BTON:Mg, and BTON:Al are shown in Figure 5c-e, indicating that the dopants can certainly improve the adsorption of water and methanol molecules.

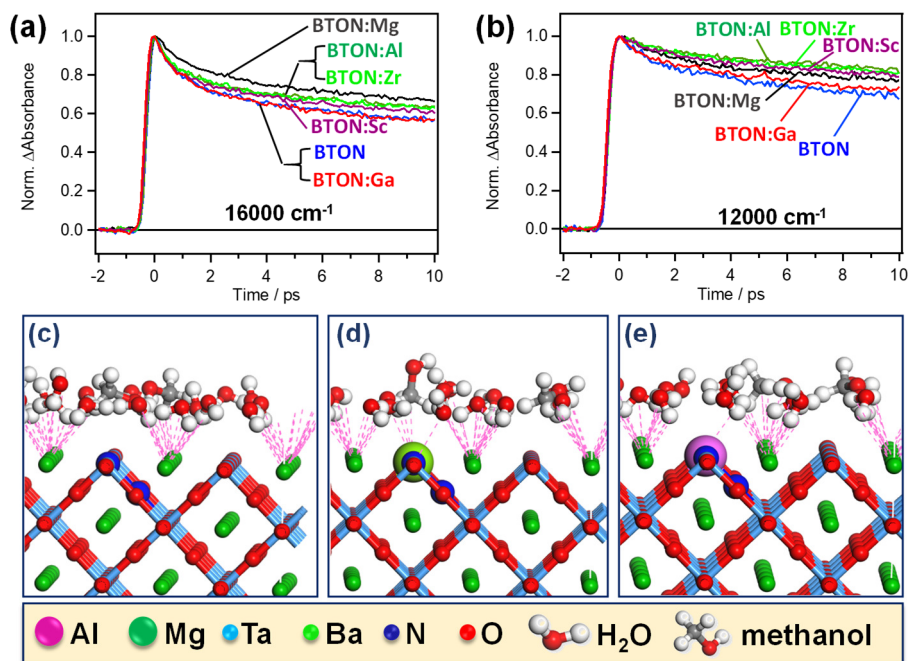


**Figure 5.** Normalized decay curves of the transient absorptions measured at 16000 cm<sup>-1</sup> (a) and 12000 cm<sup>-1</sup> (b) for pristine and cation-doped BaTaO<sub>2</sub>N photocatalysts. The samples were excited by 2 μJ,

355 nm laser pulse at 500 Hz with 90 fs duration in 20 torr N<sub>2</sub>. Close contacts of the TaO<sub>4</sub>N<sub>2</sub>-terminated (110) surfaces of (a) BTON, (b) BTON:Mg, and (c) BTON:Al.

In catalysis and electrocatalysis, interesting correlations have been reported using Sabatier's principle<sup>55,56</sup> and linear energy correlations.<sup>57-59</sup> For example, the semi-logarithmic plots of the exchange current density for proton reduction vs. the energy of the *M*-H bond (or Gibbs free energy change,  $\Delta G$ ) result in the so-called volcano-type curve.<sup>55</sup> It is anticipated that the cation doping of BaTaO<sub>2</sub>N can influence the surface chemical termination and improve the interactions of reaction intermediates, which have a significant impact on the kinetics of photocatalytic water splitting.<sup>48</sup> In a first approximation, molecular dynamics (MD) was applied as a simple, time-saving, and economic calculation method to gain insights into the respective effect of cation doping (Al<sup>3+</sup>, Ga<sup>3+</sup>, Mg<sup>2+</sup>, Sc<sup>3+</sup> and Zr<sup>4+</sup>) on the properties of the BaTaO<sub>2</sub>N surfaces terminated with TaO<sub>6</sub>, TaN<sub>6</sub>, and TaO<sub>4</sub>N<sub>2</sub> octahedra.

After having discussed the differences in the photocatalytic O<sub>2</sub> and H<sub>2</sub> evolution and the interactions of water and methanol molecules with the predominant (110) surfaces, terminated with TaO<sub>6</sub>, TaN<sub>6</sub>, and TaO<sub>4</sub>N<sub>2</sub> octahedra, of BaTaO<sub>2</sub>N above, it is possible to correlate the observed trends in photocatalytic O<sub>2</sub> and H<sub>2</sub> evolution with the energy changes of the adsorbed chemical species on pristine and cation-doped BaTaO<sub>2</sub>N photocatalysts. Similar studies have been previously reported for other catalytic systems.<sup>57-60</sup> Rationalizing these trends using a relative approach to compare the photocatalytic activities of cation-doped BaTaO<sub>2</sub>N photocatalysts with respect to that of pristine BTON allows to elucidate the differences in the surface reactions. In fact, by taking into account the relationship between the reaction rates of cation-doped BaTaO<sub>2</sub>N ( $r_{X\text{-BTON}}$ ) and that of pristine BTON ( $r_{\text{BTON}}$ ) at the initial stage (Table S4), the effect of the chemical environment during the photocatalytic reactions can be normalized. Then, the resulting magnitude ( $r_{X\text{-BTON}}/r_{\text{BTON}}$ ) is proportional to the effect of cation doping in BaTaO<sub>2</sub>N. The main difference between the synthesized BaTaO<sub>2</sub>N photocatalysts in photocatalytic O<sub>2</sub> and H<sub>2</sub> evolution is manifested in the reaction rates at the initial stage. In addition, the kinetics is determined by the energetic factors governing the surface chemistry

during the photocatalytic reactions. Thus, the correlation between  $\ln[(r_{X-BTON})/(r_{BTON})]$  and the relative energy ( $E$ ) difference at the rate-limiting step ( $rls$ ):  $\Delta E^r = -(E_{X-BTON} - E_{BTON})$ , must be linear,<sup>57-60</sup> where  $X = Al^{3+}$ ,  $Ga^{3+}$ ,  $Mg^{2+}$ ,  $Sc^{3+}$  or  $Zr^{4+}$ . To elucidate this, certain basic chemical kinetic arguments must be invoked.

Equations 1-3 express the  $H_2$  generation according to the Volmer, Heyrovsky and Tafel reactions, respectively:<sup>51,61,62</sup>



where  $*$  is an active site of the surface and  $H^*$  is the adsorbed hydrogen. If the formation of the adsorbed  $H^*$  species is the rate-limiting step ( $rls$ ) (Eq. 1), then the overall rate of  $H_2$  evolution can be expressed as:<sup>62</sup>

$$r = k_{rls} \theta^* [H^+] \quad (4)$$

and according to the Arrhenius equation, the rate constant is:

$$k_{rls} = k^0 \exp\left(-\frac{\Delta E}{RT}\right) \quad (5)$$

where  $k_{rls}$  and  $\theta^*$  correspond to the rate constant of the  $rls$  and the density of free active sites in the photocatalyst, respectively.  $\Delta E$  is the energy barrier for the  $rls$ ,  $k^0$  represents the frequency factor,  $R$  is the universal gas constant, and  $T$  is the absolute temperature. If it is considered that for all photocatalysts, the area available for adsorption is very large and the reaction occurs at the same initial pH, then the ratio of the reaction rates is:

$$\frac{r_{X-BTON}}{r_{BTON}} = \frac{k_{X-BTON}^0}{k_{BTON}^0} \exp\left[-\frac{(E_{X-BTON} - E_{BTON})}{RT}\right] \quad (6)$$

It supports the proposed linearization:  $\ln[(r_{X-BTON})/(r_{BTON})]$  vs.  $-(E_{X-BTON} - E_{BTON})$  plot (see Eq. 7).

$$\ln\left(\frac{r_{X-BTON}}{r_{BTON}}\right) = -\ln\left(\frac{k_{X-BTON}^0}{k_{BTON}^0}\right) - \frac{(E_{X-BTON} - E_{BTON})}{RT} \quad (7)$$

It is expected that the cation doping in  $BaTaO_2N$  can change the energy of the  $rls$  in the following ways:  $E_{X-BTON} < E_{BTON}$  or  $E_{X-BTON} > E_{BTON}$ , and then, the significant differences are manifested with the changes of the slope in the  $\ln[(r_{X-BTON})/(r_{BTON})]$  vs.  $\Delta E^r$  plot, where  $\Delta E^r = -(E_{X-BTON} - E_{BTON})$  is

the relative energy difference of the key adsorbed intermediate. This magnitude is proportional to the energy barrier of the *r*/*s*. Furthermore, as the ordinate axis is proportional to the relative reaction rate ( $\ln[(r_{X-BTON})/(r_{BTON})]$ ), it is possible to discriminate the cation-doped BaTaO<sub>2</sub>N photocatalysts, which exhibited the higher photocatalytic activities than the BTON:  $\ln[(r_{X-BTON})/(r_{BTON})] > 0$ , and showed a deterioration in the overall photocatalytic activity:  $\ln[(r_{X-BTON})/(r_{BTON})] < 0$ .

Figures 6a-c show the dependence of  $\ln[(r_{X-BTON})/(r_{BTON})]$  on the photocatalytic H<sub>2</sub> evolution over BaTaO<sub>2</sub>N photocatalysts as a function of the relative energy difference for H<sup>\*</sup> ( $\Delta E_{H^*}^r$ ) of the BaTaO<sub>2</sub>N surfaces terminated with TaO<sub>6</sub>, TaN<sub>6</sub>, and TaO<sub>4</sub>N<sub>2</sub> octahedra. The appearance of the V-type plot for H<sub>2</sub> evolution shows the differences in pristine and cation-doped BaTaO<sub>2</sub>N photocatalysts. First, it should be noted that all cation-doped BaTaO<sub>2</sub>N photocatalysts are photocatalytically more active than the BTON, which corresponds to the positive values for  $\ln[(r_{X-BTON})/(r_{BTON})]$ . Second, the results are categorized into two groups: (i)  $E_{X-BTON} < E_{BTON}$  in the BTON:Al and BTON:Ga photocatalysts yields a negative slope:  $d\{\ln[(r_{X-BTON})/(r_{BTON})] \}/d[(\Delta E_{H^*}^r)] < 0$  when the atomic number of the dopant is increased, and (ii)  $E_{X-BTON} > E_{BTON}$  in the BTON:Mg, BTON:Sc, and BTON:Zr photocatalysts leads to a positive slope:  $d\{\ln[(r_{X-BTON})/(r_{BTON})] \}/d[(\Delta E_{H^*}^r)] > 0$  when the atomic number of the dopant is decreased. It is noteworthy that a satisfactory match for all dopants was obtained for the BaTaO<sub>2</sub>N surfaces terminated with TaO<sub>6</sub> octahedra. Nevertheless, the BTON:Zr surface terminated with TaO<sub>4</sub>N<sub>2</sub> octahedra and BTON:Mg surface terminated with TaN<sub>6</sub> and TaO<sub>4</sub>N<sub>2</sub> octahedra resulted in trend deviations possibly due to simplifications in MD calculations. In addition, the obtained slopes (Table S4) change as a function of the surface chemical termination of BaTaO<sub>2</sub>N. For the BTON:Al and BTON:Ga photocatalysts, it is slope (TaO<sub>6</sub>) > slope (TaN<sub>6</sub>) > slope (TaO<sub>4</sub>N<sub>2</sub>), and for the BTON:Mg, BTON:Sc, and BTON:Zr photocatalysts, the result is slope (TaN<sub>6</sub>) > slope (TaO<sub>6</sub>) > slope (TaO<sub>4</sub>N<sub>2</sub>).

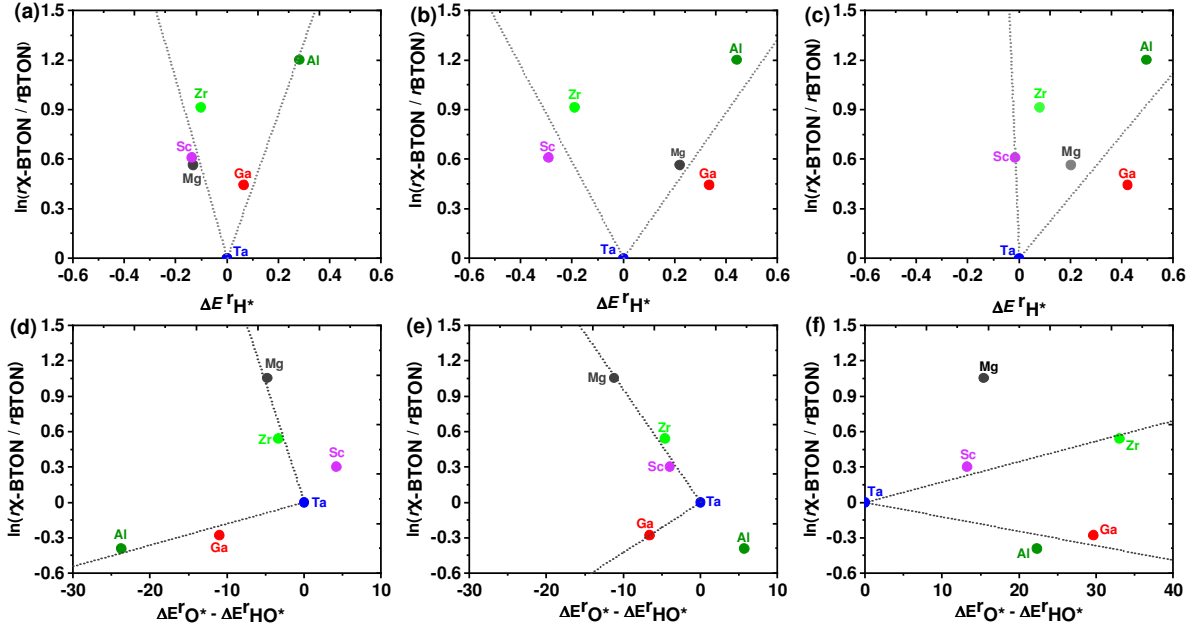


**Figure 6.** (top)  $\ln[(r_{X-BTON})/(r_{BTON})]$  vs.  $(\Delta E^T_{H^*})$  plots for  $H_2$  evolution of pristine and cation-doped  $BaTaO_2N$  photocatalysts with surfaces terminated with (a)  $TaO_6$ , (b)  $TaN_6$ , and (c)  $TaO_4N_2$  octahedra. Adsorbed intermediate is  $H^*$ . (bottom)  $\ln[(r_{X-BTON})/(r_{BTON})]$  vs.  $(\Delta E^T_{O^*} - \Delta E^T_{HO^*})$  plot for  $O_2$  evolution of pristine and cation-doped  $BaTaO_2N$  photocatalysts with surfaces terminated with (d)  $TaO_6$ , (e)  $TaN_6$ , and (f)  $TaO_4N_2$  octahedra. Adsorbed intermediates are  $O^*$  and  $HO^*$ .

Even though the  $O_2$  evolution involves a more complex mechanism with a greater number of intermediates adsorbed and electrons transferred than the  $H_2$  evolution, it is interesting to explore the trends emerging from the relative kinetic analysis. It is well documented that the difference in Gibbs energies of intermediates  $O^*$  and  $HO^*$  ( $\Delta G_{O^*} - \Delta G_{HO^*}$ ) can be used as a reaction descriptor to predict the  $O_2$  evolution activity.<sup>49,63</sup> Hence, it is expected that the correlation using the adsorption energy difference of  $O^*$  and  $HO^*$  ( $\Delta E^T_{O^*} - \Delta E^T_{HO^*}$ ) allows summarizing the trends in pristine and cation-doped  $BaTaO_2N$  photocatalysts. Equations 8-11 indicate the  $O_2$  evolution pathways.<sup>48,49</sup>



Figures 6d-f show the  $\ln[(r_{X-BTON})/(r_{BTON})]$  vs.  $(\Delta E^T_{O^*} - \Delta E^T_{HO^*})$  plots for  $O_2$  evolution. The positive values of  $\ln[(r_{X-BTON})/(r_{BTON})]$  correspond to the higher reaction rates of BTON, BTON:Mg,

BTON:Sc, and BTON:Zr photocatalysts at the initial stage, while the negative values represent the lower reaction rates of BTON:Al and BTON:Ga photocatalysts. The oxidation of water leads to the formation of hydroxyl radicals, suggesting the possibility of obtaining the linear energy-performance relationships.<sup>64,65</sup> In fact, the kinetics of photocatalytic O<sub>2</sub> evolution is governed by the number of electrons transferred corresponding to the potential, which is established at the interface.<sup>66</sup> This depends on the dynamics of holes, their accumulation, and the adsorbed intermediates.<sup>66-68</sup> Furthermore, the oxidation photocurrent was previously reported using the BaTaO<sub>2</sub>N-based electrodes, resulting in the limited signals at low overpotentials due to energy losses stemmed from the recombination of photogenerated charge carriers.<sup>12</sup> Thus, the linear trends with respect to O\* and HO\* in Figure 6 are consistent with slow kinetics during the water oxidation reaction. In fact, in the water splitting reaction using BaTaO<sub>2</sub>N photocatalysts, the important role of all adsorbed oxygen species (HO\*, O\*, and HOO\*) was highlighted<sup>48</sup> in addition to the determining role of electrochemical polarization.<sup>12,15,22,48,69</sup>

The experimental results of O<sub>2</sub> evolution using BaTaO<sub>2</sub>N photocatalysts suggest that although these materials achieve the oxidation of water under visible light irradiation without the need for electrochemical assistance, the reaction rate at the interface is slow and continuously improved with loading a cocatalyst.<sup>70</sup> The linear energy-performance relationship is a consequence of the correlation between the kinetic and thermodynamic effects during the redox reaction.<sup>57,58</sup> The use of adsorption energy as a descriptor allowed to reveal the effect of cation doping on BaTaO<sub>2</sub>N despite the presence of a cocatalyst. In all cases, the chemical nature of the cocatalysts and their interactions with the photocatalyst have an impact on improving the overall photocatalytic performance.<sup>70,71</sup> Further studies are being conducted to describe the adsorption energy-performance correlation in relation to the effects of defects, cocatalysts, doping content, the coverage of reactive species, and properties of the photocatalysts.<sup>48,71-73</sup> It is also observed that the change in slope in Figure 6 reveals the difference between the BaTaO<sub>2</sub>N photocatalysts due to the difference in dopant type used and surface chemical termination considered. The deviations observed in the BTON:Sc, BTON:Al, and BTON:Mg photocatalysts with TaO<sub>6</sub>, TaN<sub>6</sub>, and TaO<sub>4</sub>N<sub>2</sub> surface chemical terminations possibly due to

simplifications and the level of MD calculations. Nevertheless, the linear trends with good correlation and the significant slope changes are resolved for each photocatalyst (Table S4). The results of the slopes in O<sub>2</sub> evolution indicate the changes as a function of surface chemical termination. That is, for the BTON:Al and BTON:Ga photocatalysts, the slopes increase as: slope (TaO<sub>6</sub>) < slope (Ta<sub>2</sub>N<sub>6</sub>) < slope (TaO<sub>4</sub>N<sub>2</sub>), whereas for the BTON:Mg, BTON:Sc, and BTON:Zr photocatalysts, the slopes decrease in the following order: slope (TaO<sub>6</sub>) > slope (Ta<sub>2</sub>N<sub>6</sub>) > slope (TaO<sub>4</sub>N<sub>2</sub>). As is known, it is necessary to systematize the kinetic improvements in water splitting using TaON- and BaTaO<sub>2</sub>N-based photocatalysts.<sup>15,22,71</sup> By applying the relative kinetic analysis:  $\ln[(r_{X\text{-BTON}})/(r_{\text{BTON}})]$  vs.  $\Delta E^{\text{T}}$ , it was possible to distinguish the effects of cation doping (Al<sup>3+</sup>, Ga<sup>3+</sup>, Mg<sup>2+</sup>, Sc<sup>3+</sup>, and Zr<sup>4+</sup>) and surface chemical termination (TaO<sub>6</sub>, Ta<sub>2</sub>N<sub>6</sub>, and TaO<sub>4</sub>N<sub>2</sub>) on the key adsorbed chemical species, specifically O\*, HO\*, and H\*, during the photocatalytic O<sub>2</sub> and H<sub>2</sub> evolution over BaTaO<sub>2</sub>N.

Finally, it has been argued that in the water splitting reaction over BaTaO<sub>2</sub>N-based photocatalysts, it is possible that the kinetics of electron transfer reactions are slow, and the concentration of minority carriers around the surface is increased to very high values.<sup>74</sup> This phenomenon would modify the potential drop across the Helmholtz layer in the electrolyte, leading to “unpinning the edge of the band”.<sup>74,75</sup> Then, under these conditions, the phenomena that occur between the photocatalyst surface and the adsorbed intermediates could play a determining role. The role of surface phenomena is evidenced through the linear adsorption energy-performance correlations presented in Figure 6. This can be interpreted as a consequence derived from the dynamics in which the charge carriers are involved in each BaTaO<sub>2</sub>N photocatalyst, which agrees well with the changes observed in the results of the transient absorption spectroscopy measurements. The analysis of such physicochemical trends leads to a better understanding of photocatalyst nature, reaction kinetics, and designing the photocatalytic materials for future application.

#### 4. CONCLUSIONS

In summary, BaTaO<sub>2</sub>N was modified by a 5% *B*-site-selective doping of aliovalent metal cations (Al<sup>3+</sup>, Ga<sup>3+</sup>, Mg<sup>2+</sup>, Sc<sup>3+</sup>, and Zr<sup>4+</sup>) to be effective in sacrificial visible-light-induced photocatalytic H<sub>2</sub> and O<sub>2</sub> evolution. Since no significant changes in crystal structure, crystal morphology, and light



absorption were observed upon doping, the difference in the photocatalytic O<sub>2</sub> and H<sub>2</sub> evolution over pristine and cation-doped BaTaO<sub>2</sub>N photocatalysts was stemmed from the varying optoelectronic and surface properties. Particularly, the BTON:Mg and BTON:Al independently exhibited the highest amounts (in 5 h) of evolved O<sub>2</sub> (503.6 μmol) and H<sub>2</sub> (117.4 μmol), respectively, whereas the BTON:Zr showed the high photocatalytic activities in both O<sub>2</sub> (446.8 μmol) and H<sub>2</sub> (80.4 μmol) half reactions due to the altered potentials of the valence and conduction bands and an increased density of charge carriers. The highest H<sub>2</sub> reaction rate of 21.92 μmol·h<sup>-1</sup> at AM1.5 G illumination (200 mW·cm<sup>-2</sup>) was achieved using Al dopant. The kinetic V-type plots in H<sub>2</sub> evolution and the linear energy-performance correlations in O<sub>2</sub> evolution were observed using the relative kinetic analysis:  $\ln[(r_{X-BTON})/(r_{BTON})]$  vs.  $-(E_{X-BTON} - E_{BTON})$  plot. The experimental photocatalytic reaction rates were satisfactorily described using the adsorption energies of intermediates (H\* for H<sub>2</sub> evolution and HO\* and O\* for O<sub>2</sub> evolution) estimated by molecular dynamics calculations, rationalizing the effects of aliovalent metal cation doping (Al<sup>3+</sup>, Ga<sup>3+</sup>, Mg<sup>2+</sup>, Sc<sup>3+</sup>, and Zr<sup>4+</sup>) and surface chemical termination (TaO<sub>6</sub>, TaN<sub>6</sub>, and TaO<sub>4</sub>N<sub>2</sub>) of BaTaO<sub>2</sub>N.

## ASSOCIATED CONTENT:

### Supporting Information

The Supporting Information is available free of charge on the ACS Publications website at DOI:

TEM and HRTEM images and SAED patterns, XPS survey spectra, XPS valence band spectra, and energy-level diagrams of pristine and cation-doped BaTaO<sub>2</sub>N photocatalysts. Computational method, the electronic band structures, and total and partial density of states of pristine and cation-doped BaTaO<sub>2</sub>N photocatalysts. Transient absorption spectroscopy measurements, and transient absorption spectra of pristine and cation-doped BaTaO<sub>2</sub>N photocatalysts. Field density distribution and close contacts (a scaled sum of van der Waals radii) of water and methanol molecules on the predominant (110) surfaces terminated with TaO<sub>6</sub>, TaN<sub>6</sub>, and TaO<sub>4</sub>N<sub>2</sub> octahedra of pristine and cation-doped BaTaO<sub>2</sub>N photocatalysts. Masses of chemical reactants used for the synthesis of pristine and cation-doped BaTaO<sub>2</sub>N photocatalysts. Photocatalytic reaction rates for H<sub>2</sub> and O<sub>2</sub> evolution at the initial stage.

Adsorption energies of H<sub>2</sub>O, H<sub>2</sub>O+methanol, H<sub>2</sub>, O<sub>2</sub>, and intermediates (H\* for H<sub>2</sub> evolution and HO\*, O\* and HOO\* for O<sub>2</sub> evolution) on pristine and cation-doped BaTaO<sub>2</sub>N surfaces terminated with TaO<sub>6</sub>, TaN<sub>6</sub>, and TaO<sub>4</sub>N<sub>2</sub> octahedra. Slopes and  $R^2$  obtained for  $\ln[(r_{\text{X-BTON}})/(r_{\text{BTON}})]$  vs.  $\Delta E^{\text{T}}$  plot in H<sub>2</sub> evolution ( $\Delta E^{\text{T}} = \Delta E^{\text{T}}_{\text{H}^*}$ ) and O<sub>2</sub> evolution ( $\Delta E^{\text{T}} = \Delta E^{\text{T}}_{\text{O}^*} - \Delta E^{\text{T}}_{\text{HO}^*}$ ).

## ACKNOWLEDGMENTS:

This work was supported by the Artificial Photosynthesis Project of the New Energy and Industrial Technology Development Organization (NEDO). This project received funding from the European Union's Horizon 2020 research and innovation programme under the Marie Skłodowska-Curie grant agreement no. 793882. The authors would like to thank Professor Kazunari Domen for rendering the experimental facility for the evaluation of photocatalytic H<sub>2</sub> and O<sub>2</sub> evolution. Professor Nobuyuki Zettsu and Ms. Reiko Shiozawa from Shinshu University, Japan, are acknowledged for their kind assistance in XPS analysis.

## REFERENCES:

- (1) Kageyama, H.; Hayashi, K.; Maeda, K.; Attfield, J. P.; Hiroi, Z.; Rondinelli, J. M.; Poeppelmeier, K. R. Expanding Frontiers in Materials Chemistry and Physics With Multiple Anions. *Nature Commun.* **2018**, *9*, 772.
- (2) Tripathi, T. S.; Karppinen, M. Mixed-Anion Compounds: An Unexplored Playground for ALD Fabrication. *Adv. Mater. Interfaces* **2021**, *8*, 2100146.
- (3) Miyoshi, A.; Maeda, K. Recent Progress in Mixed-Anion Materials for Solar Fuel Production. *Sol. RRL* **2021**, *5*, 2000521.
- (4) Pilania, G.; Ghosh, A.; Hartman, S. T.; Mishra, R.; Stanek, C. R.; Uberuaga, B. P. Anion Order in Oxysulfide Perovskites: Origins and Implications. *npj Comput. Mater.* **2020**, *6*, 71.
- (5) Cornelius, S.; Colombi, G.; Nafezarefi, F.; Schreuders, H.; Heller, R.; Munnik, F.; Dam, B. Oxyhydride Nature of Rare-Earth-Based Photochromic Thin Films. *J. Phys. Chem. Lett.* **2019**, *10*, 1342–1348.
- (6) Kabbour, H.; Sayede, A.; Saitzek, S.; Lefèvre, G.; Cario, L.; Trentesaux, M.; Roussel, P. Structure of the Water-Splitting Photocatalyst Oxysulfide  $\alpha$ -LaOInS<sub>2</sub> and *Ab Initio* Prediction of New Polymorphs. *Chem. Commun.* **2020**, *56*, 1645–1648.
- (7) Yang, M.; Oró-Solé, J.; Rodgers, J. A.; Jorge, A. B.; Fuertes, A.; Attfield, J. P. Anion Order in Perovskite Oxynitrides. *Nature Chem.* **2011**, *3*, 47–52.
- (8) Fuertes, A. Nitride Tuning of Transition Metal Perovskites. *APL Mater.* **2020**, *8*, 020903.
- (9) Ebbinghaus, S. G.; Abicht, H. P.; Dronskowski, R.; Müller, T.; Reller, A.; Weidenkaff, A. Perovskite-Related Oxynitrides – Recent Developments in Synthesis, Characterisation and Investigations of Physical Properties. *Prog. Solid State Chem.* **2009**, *37*, 173–205.

- (10) Hartman, S. T.; Thind, A. S.; Mishra, R. Tin Oxynitride-Based Ferroelectric Semiconductors for Solar Energy Conversion Applications. *Chem. Mater.* **2020**, *32*, 9542–9550.
- (11) Higashi, M.; Domen, K.; Abe, R. Fabrication of an Efficient BaTaO<sub>2</sub>N Photoanode Harvesting a Wide Range of Visible Light for Water Splitting. *J. Am. Chem. Soc.* **2013**, *135*, 10238–10241.
- (12) Ueda, K.; Minegishi, T.; Clune, J.; Nakabayashi, M.; Hisatomi, T.; Nishiyama, H.; Katayama, M.; Shibata, N.; Kubota, J.; Yamada, T.; Domen, K. Photoelectrochemical Oxidation of Water Using BaTaO<sub>2</sub>N Photoanodes Prepared by Particle Transfer Method. *J. Am. Chem. Soc.* **2015**, *137*, 2227–2230.
- (13) Pihosh, Y.; Nandal, V.; Minegishi, T.; Katayama, M.; Yamada, T.; Seki, K.; Sugiyama, M.; Domen, K. Development of a Core–Shell Heterojunction Ta<sub>3</sub>N<sub>5</sub>-Nanorods/BaTaO<sub>2</sub>N Photoanode for Solar Water Splitting. *ACS Energy Lett.* **2020**, *5*, 2492–2497.
- (14) Nishimae, S.; Mishima, Y.; Nishiyama, H.; Sasaki, Y.; Nakabayashi, M.; Inoue, Y.; Katayama, M.; Domen, K. Fabrication of BaTaO<sub>2</sub>N Thin Films by Interfacial Reactions of BaCO<sub>3</sub>/Ta<sub>3</sub>N<sub>5</sub> Layers on a Ta Substrate and Resulting High Photoanode Efficiencies During Water Splitting. *Sol. RRL* **2020**, *4*, 1900542.
- (15) Seo, J.; Nakabayashi, M.; Hisatomi, T.; Shibata, N.; Minegishi, T.; Domen, K. Solar-Driven Water Splitting over a BaTaO<sub>2</sub>N Photoanode Enhanced by Annealing in Argon. *ACS Appl. Energy Mater.* **2019**, *2*, 5777–5784.
- (16) Maeda, K.; Domen, K. Water Oxidation Using a Particulate BaZrO<sub>3</sub>-BaTaO<sub>2</sub>N Solid-Solution Photocatalyst That Operates under a Wide Range of Visible Light. *Angew. Chem. Int. Ed.* **2012**, *51*, 9865–9869.
- (17) Jadhav, S.; Hasegawa, S.; Hisatomi, T.; Wang, Z.; Seo, J.; Higashi, T.; Katayama, M.; Minegishi, T.; Takata, T.; Peralta-Hernandez, J. M.; Torres, O. S.; Domen, K. Efficient Photocatalytic Oxygen Evolution Using BaTaO<sub>2</sub>N Obtained From Nitridation of Perovskite-Type Oxide. *J. Mater. Chem. A* **2020**, *8*, 1127–1130.
- (18) Hojamberdiev, M.; Yubuta, K.; Vequizo, J. J. M.; Yamakata, A.; Oishi, S.; Domen, K.; Teshima, K. NH<sub>3</sub>-Assisted Flux Growth of Cube-like BaTaO<sub>2</sub>N Submicron Crystals in a Completely Ionized Nonaqueous High-Temperature Solution and Their Water Splitting Activity. *Cryst. Growth Des.* **2015**, *15*, 4663–4671.
- (19) Hojamberdiev, M.; Zahedi, E.; Nurlaela, E.; Kawashima, K.; Yubuta, K.; Nakayama, M.; Wagata, H.; Minegishi, T.; Domen, K.; Teshima, K. The Cross-Substitution Effect of Tantalum on the Visible-Light-Driven Water Oxidation Activity of BaNbO<sub>2</sub>N Crystals Grown Directly by An NH<sub>3</sub>-Assisted Flux Method. *J. Mater. Chem. A* **2016**, *4*, 12807–12817.
- (20) Luo, Y.; Wang, Z.; Yamada, T.; Yubuta, K.; Suzuki, S.; Hisatomi, T.; Domen, K.; Teshima, K. Flat BaTaO<sub>2</sub>N Crystals Fabricated from K<sub>2</sub>CO<sub>3</sub>-KCl Binary Flux for Photocatalytic H<sub>2</sub> Evolution. *ACS Appl. Energy Mater.* **2020**, *3*, 10669–10675.
- (21) Luo, Y.; Suzuki, S.; Wang, Z.; Yubuta, K.; Vequizo, J. J. M.; Yamakata, A.; Shiiba, H.; Hisatomi, T.; Domen, K.; Teshima, K. Construction of Spatial Charge Separation Facets on BaTaO<sub>2</sub>N Crystals by Flux Growth Approach for Visible-Light-Driven H<sub>2</sub> Production. *ACS Appl. Mater. Interfaces* **2019**, *11*, 22264–22271.
- (22) Wang, Z.; Luo, Y.; Hisatomi, T.; Vequizo, J. J. M.; Suzuki, S.; Chen, S.; Nakabayashi, M.; Lin, L.; Pan, Z.; Kariya, N.; Yamakata, A.; Shibata, N.; Takata, T.; Teshima, K.; Domen, K. Sequential Cocatalyst Decoration on BaTaO<sub>2</sub>N Towards Highly-Active Z-Scheme Water Splitting. *Nature Commun.* **2021**, *12*, 1005.
- (23) Wang, Q.; Domen, K. Particulate Photocatalysts for Light-Driven Water Splitting: Mechanisms, Challenges, and Design Strategies. *Chem. Rev.* **2020**, *120*, 919–985.
- (24) Ham, Y.; Hisatomi, T.; Goto, Y.; Moriya, Y.; Sakata, Y.; Yamakata, A.; Kubota, J.; Domen, K. Flux-Mediated Doping of SrTiO<sub>3</sub> Photocatalysts for Efficient Overall Water Splitting. *J. Mater. Chem. A* **2016**, *4*, 3027–3033.

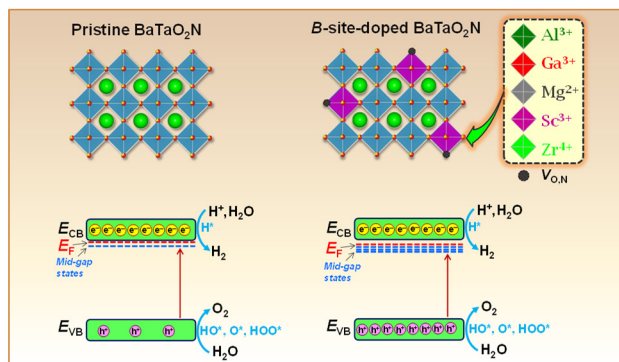
- (25) Zhang, H.; Wei, S.; Xu, X. Mg Modified BaTaO<sub>2</sub>N As An Efficient Visible-Light-Active Photocatalyst for Water Oxidation. *J. Catal.* **2020**, *383*, 135–143.
- (26) Higashi, M.; Yamanaka, Y.; Tomita, O.; Abe, R. Fabrication of Cation-Doped BaTaO<sub>2</sub>N Photoanodes for Efficient Photoelectrochemical Water Splitting Under Visible Light Irradiation. *APL Mater.* **2015**, *3*, 104418.
- (27) Takata, T.; Domen, K. Defect Engineering of Photocatalysts by Doping of Aliovalent Metal Cations for Efficient Water Splitting. *J. Phys. Chem. C* **2009**, *113*, 19386–19388.
- (28) Makuła, P.; Pacia, M.; Macyk, W. How To Correctly Determine the Band Gap Energy of Modified Semiconductor Photocatalysts Based on UV–Vis Spectra. *J. Phys. Chem. Lett.* **2018**, *9*, 6814–6817.
- (29) Sharma, S.; Kumar, P.; Chandra, R.; Singh, S. P.; Mandal, A.; Dondapati, R. S. Overview of BIOVIA materials studio, LAMMPS, and GROMACS. In: Molecular Dynamics Simulation of Nanocomposites Using BIOVIA Materials Studio, Lammmps and Gromacs (Ed. S. Sharma), Elsevier, Amsterdam, 2019, pp. 39–100.
- (30) Dubouis, N.; Grimaud, A. The Hydrogen Evolution Reaction: From Material to Interfacial Descriptors. *Chem. Sci.* **2019**, *10*, 9165–9181.
- (31) Hojamberdiev, M.; Vargas, R.; Bhati, V. S.; Torres, D.; Kadirova, Z. C.; Kumar, M. Unraveling the Photoelectrochemical Behavior of Ni-Modified ZnO and TiO<sub>2</sub> Thin Films Fabricated by RF Magnetron Sputtering. *J. Electroanal. Chem.* **2021**, *882*, 115009.
- (32) Seo, J.; Takata, T.; Nakabayashi, M.; Hisatomi, T.; Shibata, N.; Minegishi, T.; Domen, K. Mg-Zr Cosubstituted Ta<sub>3</sub>N<sub>5</sub> Photoanode for Lower-Onset-Potential Solar-Driven Photoelectrochemical Water Splitting. *J. Am. Chem. Soc.* **2015**, *137*, 12780–12783.
- (33) Ida, S.; Ishihara, T. Recent Progress in Two-Dimensional Oxide Photocatalysts for Water Splitting. *J. Phys. Chem. Lett.* **2014**, *5*, 2533–2542.
- (34) Balaz, S.; Porter, S. H.; Woodward, P. M.; Brillson, L. J. Electronic Structure of Tantalum Oxynitride Perovskite Photocatalysts. *Chem. Mater.* **2013**, *25*, 3337–3343.
- (35) Wang, Y.; Jin, S.; Pan, G.; Li, Z.; Chen, L.; Liu, G.; Xu, X. Zr Doped Mesoporous LaTaON<sub>2</sub> for Efficient Photocatalytic Water Splitting. *J. Mater. Chem. A* **2019**, *7*, 5702–5711.
- (36) Kubo, A.; Giorgi, G.; Yamashita, K. Anion Ordering in CaTaO<sub>2</sub>N: Structural Impact on the Photocatalytic Activity. Insights from First-Principles. *Chem. Mater.* **2017**, *29*, 539–545.
- (37) Hafez, A.M.; Salem, N.M.; Allam, N.K. Unravelling the Correlated Electronic and Optical Properties of BaTaO<sub>2</sub>N With Perovskite-Type Structure As a Potential Candidate for Solar Energy Conversion. *Phys. Chem. Chem. Phys.* **2014**, *16*, 18418–18424.
- (38) Kisch, H.; Bahnemann, D. Best Practice in Photocatalysis: Comparing Rates or Apparent Quantum Yields? *J. Phys. Chem. Lett.* **2015**, *6*, 1907–1910.
- (39) Monllor-Satoca, D.; Díez-García, M. I.; Lana-Villarreal, T.; Gómez, R. Photoelectrocatalytic Production of Solar Fuels with Semiconductor Oxides: Materials, Activity and Modeling. *Chem. Commun.* **2020**, *56*, 12272–12289.
- (40) Xiao, J.; Vequizo, J. J. M.; Hisatomi, T.; Rabeah, J.; Nakabayashi, M.; Wang, Z.; Xiao, Q.; Li, H.; Pan, Z.; Krause, M.; Yin, N.; Smith, G.; Shibata, N.; Brückner, A.; Yamakata, A.; Takata, T.; Domen, K. Simultaneously Tuning the Defects and Surface Properties of Ta<sub>3</sub>N<sub>5</sub> Nanoparticles by Mg-Zr Codoping for Significantly Accelerated Photocatalytic H<sub>2</sub> Evolution. *J. Am. Chem. Soc.* **2021**, *143*, 10059–10064.

- (41) Wang, S.; Pan, L.; Song, J.-J.; Mi, W.; Zou, J.-J.; Wang, L.; Zhang, X. Titanium-Defected Undoped Anatase TiO<sub>2</sub> with p-Type Conductivity, Room-Temperature Ferromagnetism, and Remarkable Photocatalytic Performance. *J. Am. Chem. Soc.* **2015**, *137*, 2975–2983.
- (42) Makaremi, M.; Grixti, S.; Butler, K. T.; Ozin, G. A.; Singh, C. V. Band Engineering of Carbon Nitride Monolayers by N-Type, P-Type, and Isoelectronic Doping for Photocatalytic Applications. *ACS Appl. Mater. Interfaces* **2018**, *10*, 11143–11151.
- (43) Zhao, Z.; Goncalves, R. V.; Barman, S. K.; Willard, E. J.; Byle, E.; Perry, R.; Wu, Z.; Huda, M. N.; Moulé, A. J.; Osterloh, F. E. Electronic Structure Basis for Enhanced Overall Water Splitting Photocatalysis with Aluminum Doped SrTiO<sub>3</sub> in Natural Sunlight. *Energy Environ. Sci.* **2019**, *12*, 1385–1395.
- (44) Chiang, T. H.; Lyu, H.; Hisatomi, T.; Goto, Y.; Takata, T.; Katayama, M.; Minegishi, T.; Domen, K. Efficient Photocatalytic Water Splitting Using Al-Doped SrTiO<sub>3</sub> Coloaded with Molybdenum Oxide and Rhodium-Chromium Oxide. *ACS Catal.* **2018**, *8*, 2782–2788.
- (45) Ng, K. H.; Minggu, L. J.; Kassim, M. B. Gallium-Doped Tungsten Trioxide Thin Film Photoelectrodes for Photoelectrochemical Water Splitting. *Int. J. Hydrog. Energy* **2013**, *38*, 9585–9591.
- (46) Wang, Y.; Zhu, D.; Xu, X. Zr-Doped Mesoporous Ta<sub>3</sub>N<sub>5</sub> Microspheres for Efficient Photocatalytic Water Oxidation. *ACS Appl. Mater. Interfaces* **2016**, *8*, 35407–35418.
- (47) An, L.; Kitta, M.; Iwase, A.; Kudo, A.; Ichikuni, N.; Onishi, H. Photoexcited Electrons Driven by Doping Concentration Gradient: Flux-Prepared NaTaO<sub>3</sub> Photocatalysts Doped with Strontium Cations. *ACS Catal.* **2018**, *8*, 9334–9341.
- (48) Lan, Z.; Vegge, T.; Castelli, I. E. Theoretical Insight on Anion Ordering, Strain, and Doping Engineering of the Oxygen Evolution Reaction in BaTaO<sub>2</sub>N. *Chem. Mater.* **2021**, *33*, 3297–3303.
- (49) Koper, M. T. M. Thermodynamic Theory of Multi-Electron Transfer Reactions: Implications for Electrocatalysis. *J. Electroanal. Chem.* **2011**, *660*, 254–260.
- (50) Wu, H. Z.; Liu, L. M.; Zhao, S. J. The Effect of Water on the Structural, Electronic and Photocatalytic Properties of Graphitic Carbon Nitride. *Phys. Chem. Chem. Phys.* **2014**, *16*, 3299–3304.
- (51) Wang, Z. T.; Wang, Y. G.; Mu, R.; Yoon, Y.; Dahal, A.; Schenter, G. K.; Glezakou, V. A.; Rousseau, R.; Lyubnitsky, I.; Dohnálek, Z. Probing Equilibrium of Molecular and Deprotonated Water on TiO<sub>2</sub>(110). *Proc. Natl. Acad. Sci. U.S.A.* **2017**, *114*, 1801–1805.
- (52) Li, B.; Wu, S.; Gao, X. Theoretical Calculations of a TiO<sub>2</sub>-Based Photocatalyst in the Field of Water Splitting: A Review. *Nanotechnol. Rev.* **2020**, *9*, 1080–1103.
- (53) Wood, B. C.; Ogitsu, T.; Schwegler, E. *Ab Initio* Modeling of Water-Semiconductor Interfaces for Photocatalytic Water Splitting: Role of Surface Oxygen and Hydroxyl. *J. Photon. Energy* **2011**, *1*, 016002.
- (54) Lin, S.; Huang, H.; Ma, T.; Zhang, Y. Photocatalytic Oxygen Evolution From Water Splitting. *Adv. Sci.* **2021**, *8*, 2002458.
- (55) Trasatti, S. Work Function, Electronegativity, and Electrochemical Behaviour of Metals. III. Electrolytic Hydrogen Evolution in Acid Solutions. *J. Electroanal. Chem.* **1972**, *39*, 163–184.
- (56) Ooka, H.; Huang, J.; Exner, K. S. The Sabatier Principle in Electrocatalysis: Basic, Limitations and Extensions. *Front. Eng. Res.* **2021**, *9*, 654460.
- (57) Dunn, H. J. Linear Free Energy Relation in Modeling Heterogeneous Catalytic Reactions. *J. Catal.* **1968**, *12*, 335–340.

- (58) Appleby, A. J.; Zagal, J. H. Free Energy Relationships in Electrochemistry: A History That Started in 1935. *J. Solid. State. Electrochem.* **2011**, *9*, 1811–1832.
- (59) Vargas, R.; Borrás, C.; Méndez, D.; Mostany, J.; Scharifker, B. R. Electrochemical Oxygen Transfer Reactions: Electrode Materials, Surface Processes, Kinetic Models, Linear Free Energy Correlations and Perspectives. *J. Solid. State. Electrochem.* **2016**, *20*, 875–893.
- (60) Dunn, H. J. Application of Linear Free Energy Relationships to Heterogeneous Catalytic Reactions. *J. Catal.* **1968**, *11*, 79–81.
- (61) Voiry, D.; Shin, H. S.; Loh, K.P.; Chhowalla, M. Low-Dimensional Catalysts for Hydrogen Evolution and CO<sub>2</sub> Reduction. *Nature. Rev.* **2018**, *2*, 1–17.
- (62) Liu, P.; Rodriguez, J. A. Catalysts for Hydrogen Evolution From the [NiFe] Hydrogenase to the Ni<sub>2</sub>P(001) Surface: The Importance of Ensemble Effect. *J. Am. Chem. Soc.* **2005**, *127*, 14871–14878.
- (63) Craig, M.; Coulter, G.; Dolan, E.; Soriano-López, J.; Mates-Torres, E.; Schmith, W.; García-Melchor, M. Universal Scaling Relations for the Rational Design of Molecular Water Oxidation Catalysis with Near-Zero Overpotential. *Nature Comm.* **2019**, *10*, 4993.
- (64) Minakata, D.; Crittenden, J. Linear Free Energy Relationships between Aqueous Phase Hydroxyl Radical Reaction Rate Constant and Free Energy of Activation. *Environ. Sci. Technol.* **2011**, *45*, 3479–3486.
- (65) Rossmeisl, J.; Qu, Z. W.; Zhu, H.; Kroes, G. J.; Norskov, J. K. Electrolysis of Water on Oxide Surfaces. *J. Electroanal. Chem.* **2007**, *607*, 83–89.
- (66) Takeuchi, S.; Takashima, M.; Takase, M.; Ohtani, B. Digitally Controlled Kinetics of Titania-Photocatalyzed Oxygen Evolution. *Chem. Lett.* **2018**, *47*, 372–376.
- (67) Fabbri, E.; Schmidt, T. J. Oxygen Evolution Reaction – The Enigma Water Electrolysis. *ACS. Catal.* **2018**, *8*, 9765–9774.
- (68) Vargas, R.; Madriz, L.; Carvajal, D.; Scharifker, B. R. Chemical Kinetics in Solar to Chemical Energy Conversion: The Photoelectrochemical Oxygen Transfer Reaction. *Energy. Rep.* **2020**, *6*, 2–12.
- (69) Wang, C.; Hisatomi, T.; Minegishi, T.; Wang, Q.; Zhong, M.; Katayama, M.; Kubota, J.; Domen, K. Synthesis of Nanostructured BaTaO<sub>2</sub>N Thin Films As Photoanodes For Solar Water Splitting. *J. Phys. Chem. C* **2016**, *120*, 15758–15764.
- (70) Hisatomi, T.; Takanabe, K.; Domen, K. Photocatalytic Water-Splitting Reaction From Catalytic and Kinetic Perspectives. *Catal. Lett.* **2015**, *145*, 95–108.
- (71) Zhang, P.; Wang, T.; Gong, J. Current Mechanistic Understanding of Surface Reactions Over Water-Splitting Photocatalysis. *Chem.* **2018**, *4*, 223–245.
- (72) Zhang, Y-Ch.; Afzal, N.; Pan.; L.; Zhang.; X.; Zuo. J-J. Structure-Activity Relationship of Defective Metal-Based Photocatalysts for Water Splitting: Experimental and Theoretical Perspectives. *Adv. Sci.* **2019**, *6*, 1900053.
- (73) Guo, Z.; Ambrosio, F.; Pasquarello, A. Evaluation of Photocatalysis for Water Splitting Through Combined Analysis of Surface Coverage and Energy-Level Alignment. *ACS Catal.* **2020**, *10*, 13186–13195.
- (74) Hojamberdiev, M.; Mora-Hernandez, J.M.; Vargas, R.; Yamakata, A.; Yubuta, K.; Heppke, E.M.; Torres-Martínez, L.M.; Teshima, K.; Lerch, M. Time-Retrenched Synthesis of BaTaO<sub>2</sub>N by Localizing an NH<sub>3</sub> Delivery System for Visible-Light-Driven Photoelectrochemical Water Oxidation at Neutral pH: Solid-State Reaction or Flux Method? *ACS Appl. Energy Mater.* **2021**, *4*, 9315–9327.

(75) Peter, L.M.; Walker, A.B.; Bein, T.; Hufnagel, A.G.; Kondofersky, I. Interpretation of Photocurrent Transients at Semiconductor Electrodes: Effects of Band-Edge Unpinning, *J. Electroanal. Chem.* **2020**, 872, 114234.

## For Table of Contents Use Only



To enhance sacrificial visible-light-induced photocatalytic  $\text{H}_2$  and  $\text{O}_2$  evolution over  $\text{BaTaO}_2\text{N}$ , 5% *B*-site-selective doping of aliovalent metal cations was explored.  $\text{BTON:Mg}$  and  $\text{BTON:Al}$  independently exhibited the highest amounts (in 5 h) of evolved  $\text{O}_2$  ( $503.6 \mu\text{mol}$ ) and  $\text{H}_2$  ( $117.4 \mu\text{mol}$ ), respectively, whereas the  $\text{BTON:Zr}$  showed the high photocatalytic activities in both  $\text{O}_2$  ( $446.8 \mu\text{mol}$ ) and  $\text{H}_2$  ( $80.4 \mu\text{mol}$ ) half reactions.